Spatially varying dynamical properties of turbid media probed with diffusing temporal light correlation

D. A. Boas* and A. G. Yodh

Department of Physics, University of Pennsylvania, Philadelphia, Pennsylvania 19104

The diffusion of correlation is used to detect, localize, and characterize dynamical and optical spatial inhomogeneities in turbid media and is accurately modeled by a correlation diffusion equation. We demonstrate experimentally and with Monte Carlo simulations that the transport of correlation can be viewed as a correlation wave {analogous to a diffuse photon-density wave [Phys. Today **48**, 34 (1995)]} that propagates spherically outward from sources and scatters from macroscopic spatial variations in dynamical and/or optical properties. We demonstrate the utility of inverse scattering algorithms for reconstructing images of the spatially varying dynamical properties of turbid media. The biomedical applicability of this diffuse correlation probe is illustrated in studies of the depth of burned tissues. © 1997 Optical Society of America. [S0740-3232(97)02301-6]

1. INTRODUCTION

The potential to acquire information about tissue optical and dynamical properties noninvasively offers exciting possibilities for medical imaging. For this reason, the diffusion of near-infrared photons in turbid media has been the focus of substantial recent research.[1–4] Applications range from pulse oximetry[5–10] to tissue characterization[11,12] to imaging of breast and brain tumors[13–15] to probing blood flow.[16–19]

When a photon scatters from a moving particle its carrier frequency is Doppler shifted by an amount proportional to the speed of the scattering particle and is dependent on the scattering angle relative to the velocity of the scatterer. Measurements of the small frequency shifts caused by Doppler scattering events make possible the noninvasive study of particle motions and density fluctuations in a wide range of systems, such as the Brownian motion of suspended macromolecules,[20–23] velocimetry of flow fields,[24–27] and *in vivo* blood flow monitoring.[28–30]

The methods for using light to study motions by means of speckle fluctuations have appeared with numerous names over the years.[22,23,31–35] In most of these intensity fluctuation or light-beating measurements the quantity of interest is the electric-field temporal autocorrelation function $G_1(\mathbf{r}, \tau) = \langle \mathbf{E}(\mathbf{r}, t)\mathbf{E}^*(\mathbf{r}, t + \tau) \rangle$ or its Fourier transform $I(\mathbf{r}, \omega)$. Here the angle brackets $\langle \ \rangle$ denote ensemble averages (or averages over time t for most systems of practical interest), $\mathbf{r}$ represents the position of the detector, and τ is the correlation time. Both methodologies are sensitive and useful.[36] In most practical situations one measures a light-intensity temporal correlation function or Fourier equivalent and then applies the Bloch–Siegert relation[32,34,37] to deduce the field correlation functions or Fourier equivalent. The field correlation function is explicitly related to the motions within the sample under study. Since our theoretical formulation and measurements have generally focused on the time-

domain picture,[38–40] we shall continue to adopt that picture throughout this paper. We note, however, that a line-shape analysis of the light spectrum obtained by the frequency-domain instruments will provide entirely equivalent information.

The photon correlation methods and Fourier equivalents have been used with great success in optically thin samples. More recently there has been a greater effort to quantify this class of signal from turbid samples. For example, the development and the application of diffusing-wave spectroscopy (DWS),[32–35] whereby temporal correlations of highly scattered light probe dynamical motions in homogeneous complex fluids such as colloids,[41–47] foams,[48,49] emulsions,[50] and gels.[51] In the medical community application of the theory of Bonner and Nossal[30] has led to a better accounting of the spectral broadening of a light field as it travels through a highly scattering media while experiencing some scattering events from stationary scatterers and some from moving cells.

Recently we have developed and applied a formalism for the treatment of light fluctuation transport in heterogeneous highly scattering media. We have introduced a diffusion equation for the migration of the electric-field temporal autocorrelation function through turbid media.[38] The so-called correlation diffusion equation is a generalization of the photon diffusion equation that encompasses the well-known propagation of diffuse photon-density waves[1]; however, it also provides a mathematical description that accounts for the effects of motional fluctuations on the spectrum (or the temporal correlations) of propagating diffusive waves. The equation includes the effects of absorption, scattering, and dynamical motions. Importantly, it provides a natural framework when one is considering turbid media with spatially varying properties. The new approach is formally similar to much of the research being carried out in the photon migration community.[1–4] Thus it will be possible to empower many

of the technical advances already made toward functional imaging and spectroscopy with diffusing light, and it will be possible to integrate a qualitatively new technology into existing optical instrumentation.

In this paper we have attempted to develop thoroughly and to apply ideas that we have presented in earlier papers.[38,40] The paper is organized as follows. Section 2 reviews the theory of photon correlation spectroscopy from the single-scattering regime to the multiple-scattering regime. Section 3 describes the setup for our experimental measurements and the approach for our Monte Carlo simulations. The experimental and the simulation results are discussed in Sections 4 and 5, respectively. Section 6 demonstrates, with an animal model, that tissue burns varying in depth by 100 μm can be distinguished. A summary is given in Section 7, which is followed by a detailed derivation, given in Appendix A, of the correlation diffusion equation from the correlation transport equation.

2. THEORY

When a beam of laser light with uniform intensity migrates through a turbid sample, the emerging intensity pattern is not uniform but will instead be composed of many bright and dark spots called speckles. The variations arise because the photons that emerge from the sample have traveled along different paths that interfere constructively and destructively at different detector positions. If the scattering particles in the turbid medium are moving, the speckle pattern will fluctuate in time.

For the turbid medium, the time scale of the speckle intensity fluctuations depends on the number of interactions that detected photons have had with moving scattering particles. In this section we briefly review the theory for temporal field autocorrelation functions of light scattered from optically dilute systems, i.e., photons scat-

ter no more than once before being detected. We then discuss the extension of single-scattering theory to systems that multiply scatter light. After a brief review of DWS, we describe in detail a new and general description based on the transport of correlation in optically dense systems.

A. Single Scattering

Consider the system depicted in Fig. 1. A beam of coherent light is incident upon a dilute suspension of identical scattering particles. The light scattered by an angle θ is detected by a photodetector. The electric field reaching the detector is a superposition of all the scattered electric fields:

$$\mathbf{E} = \mathbf{E}_o F(q) \sum_{n=1}^{N} \exp(i\mathbf{k}_{\text{in}} \cdot \mathbf{r}_n) \exp[i\mathbf{k}_{\text{out}} \cdot (\mathbf{R}_d - \mathbf{r}_n)]$$

$$= \mathbf{E}_o F(q) \exp(i\mathbf{k}_{\text{out}} \cdot \mathbf{R}_d) \sum_{n=1}^{N} \exp(-i\mathbf{q} \cdot \mathbf{r}_n). \tag{1}$$

Here $\mathbf{E}$ is the electric field reaching the detector at position $\mathbf{R}_d$, $\mathbf{E}_o$ is the amplitude of the incident field, and $F(q)$ is the form factor for light to receive a momentum transfer of $\mathbf{q} = \mathbf{k}_{\text{out}} - \mathbf{k}_{\text{in}}$, where $\mathbf{k}_{\text{out}}$ and $\mathbf{k}_{\text{in}}$ are the output and the input wave vectors, respectively, and $|\mathbf{q}| = 2k_o \sin \theta/2$, with $k_o = |k_{\text{in}}| = |k_{\text{out}}|$. For simplicity we neglect polarization effects and assume randomly positioned and oriented scatterers. Under these conditions the differential scattering cross section is dependent only on the magnitude of $\mathbf{q}$. The summation is over the N particles in the scattering volume, and $\mathbf{r}_n$ is the position of each particle. We can see from Eq. (1) that the phase of each scattered wave depends on the momentum transfer (i.e., scattering angle) and on the position of the particle. In a disordered system the particles are randomly distributed, resulting in random constructive and de-
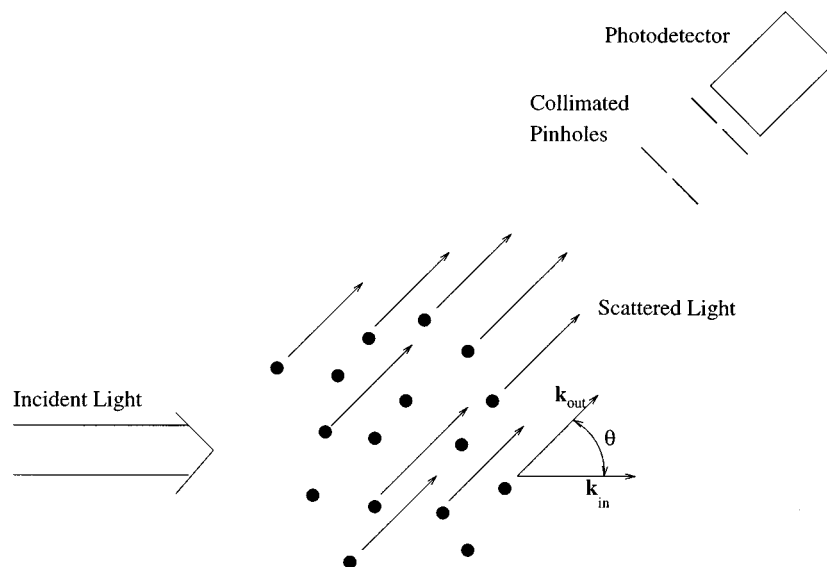

Fig. 1. Schematic of system in which light is incident upon a dilute suspension of scatterers. The suspension is dilute enough that photons are scattered no more than once. Scattered light is measured at an angle θ defined by two pinholes and is monitored with a photodetector.

structive interference at the detector. Displacing a single particle changes the interference and thus the intensity reaching the detector.

For particles that are undergoing random relative motion, e.g., Brownian motion, the phases of the individual scattered waves are changing randomly and independently of the other scattered waves. The intensity at the detector will thus fluctuate. The time scale of the intensity fluctuations is related to the rate at which the phase of the scattered waves is changing and thus depends on the motion of the scattering particles and on the momentum transfer **q**. The intensity fluctuations are more rapid at larger scattering angles and for faster moving particles.

By monitoring the intensity fluctuations it is possible to derive information about the motion of the scattering particles. There are two standard experimental approaches. One uses the unnormalized temporal intensity autocorrelation function

$$G_2(\tau) = \langle I(t)I(t + \tau)\rangle, \qquad (2)$$

where $I(t)$ is the light intensity at time t and $\langle \ \rangle$ denotes an ensemble average. For an ergodic system, an ensemble average is equivalent to a time average, and thus $G_2(\tau)$ can be obtained by a temporal average of the correlation function. The other method probes the power spectrum of the detected intensity, $S(\omega)$, and is related to the intensity temporal correlation function by[30,36,52,53]

$$S(\omega) = \frac{\langle I\rangle^2}{2\pi} \int_{-\infty}^{\infty} \cos(\omega\tau)[g_2(\tau) - 1]\mathrm{d}\tau, \qquad (3)$$

where $g_2(\tau) = G_2(\tau)/\langle I\rangle^2$ is the normalized temporal intensity correlation function and $\langle I\rangle$ is the average intensity.

In our discussion we focus on measurements of the temporal correlation function. However, it should be remembered that the information content of $S(\omega)$ is entirely equivalent. Most calculations of the effects of sample fluctuations on scattered light yield expressions for the temporal electric-field correlation function, $G_1(\tau) = \langle \mathbf{E}(0)\mathbf{E}^*(\tau)\rangle$. For Gaussian processes $G_2(\tau)$ and $G_1(\tau)$ are related by the Siegert relation[32,34,37]

$$G_2(\tau) = \langle I\rangle^2 + \beta|G_1(\tau)|^2, \qquad (4)$$

where $\langle I\rangle$ is the ensemble-averaged intensity. β is a parameter that depends on the number of speckles detected and on the coherence length and stability of the laser. β thus depends on the experimental setup. For an ideal experimental setup $\beta = 1$. See Refs. 54 and 55 for further discussion on β.

The normalized temporal field correlation function is

$$g_1(\tau) = \frac{\langle \mathbf{E}(0)\mathbf{E}^*(\tau)\rangle}{\langle |\mathbf{E}(0)|^2\rangle}. \qquad (5)$$

Using Eq. (1) for the scattered electric field and assuming that the particles move independently and are uniformly distributed, one can show that[22,23,31]

$$g_1(\tau) = \exp[-\tfrac{1}{6}\, q^2\langle\Delta r^2(\tau)\rangle]. \qquad (6)$$

Here $\langle\Delta r^2(\tau)\rangle$ is the mean-squared displacement of the scattering particles in time t, where D_B is the Brownian

diffusion coefficient. The correlation function decays exponentially with a decay time roughly of the order of the amount of time that it takes a scattering particle to move q^{-1}.

If the scatterers are undergoing Brownian motion, then $\langle\Delta r^2(\tau)\rangle = 6D_B\tau$, where D_B is the Brownian diffusion coefficient. For the case of random flow in which the particle velocity distribution is isotropic and has a Gaussian distribution, $\langle\Delta r^2(\tau)\rangle = \langle\Delta V^2\rangle\tau^2$, where $\langle\Delta V^2\rangle$ is the mean-square velocity. Shear flow and turbulence have also been studied.[24–27,56]

B. Multiple Scattering: Diffusing-Wave Spectroscopy

When the concentration of particles is increased, light is scattered many times before it emerges from the system (see Fig. 2). The photons reaching the detector typically follow various trajectories of differing path lengths through the medium. Under these conditions the correlation function can be calculated within the framework of DWS.[32–35]

In the context of DWS, the normalized field correlation function of light that has migrated a path length s through a highly scattering system is

$$g_1^{(s)}(\tau) = \exp[-\tfrac{1}{3}\, k_o^2\langle\Delta r^2(\tau)\rangle(s/l^*)], \qquad (7)$$

where $l^* = 1/\mu_s'$ is the photon random-walk step length, which is the reciprocal of the reduced scattering coefficient, and k_o is the light wave number in the medium. Once again it is necessary to assume that the particles move independently and are uniformly distributed.

Equation (7) has a form similar to that of the single-scattering result, Eq. (6), except its exponential decay rate is multiplied by the number of random-walk steps experienced by the photon in the medium, s/l^*, and the appearance of k_o instead of q reflects the fact that there is no longer a well-defined scattering angle in the problem. The correlation function for trajectories of longer length will decay more quickly, permitting the motion of scattering particles to be probed on ever shorter time scales.

Generally, a continuous-wave (cw) laser is used to illuminate the sample, and the full distribution of path lengths contributes to the decay of the correlation function. Under these conditions, the field correlation function is given by
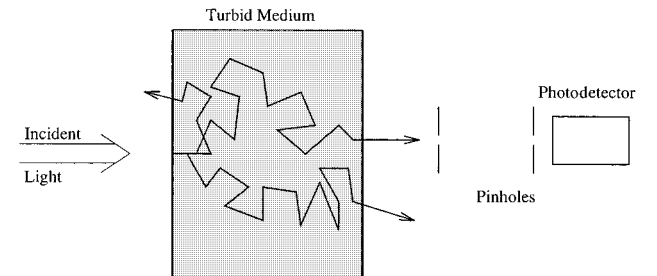

Fig. 2. Schematic of system in which light is incident upon a concentrated suspension of scatterers. Photons on average are scattered many times before emerging from the system. A single speckle of transmitted light is imaged with pinholes (or is gathered by a single-mode fiber) and is monitored with a photodetector.

$$g_1(\tau) = \int_0^\infty P(s) \exp\left[-{}^1\!/{}_3\, k_o^{\,2} \langle \Delta r^2(\tau) \rangle \frac{s}{l^*} \right] ds, \qquad (8)$$

where $P(s)$ is the normalized distribution of path lengths. This relation is valid given the assumption that the laser coherence length is much longer than the width of the photon path-length distribution.[55] The path-length distribution, $P(s)$, is found from the photon diffusion equation for the particular source–detector geometry used here. $g_1(\tau)$ has been calculated for various geometries, including semi-infinite and slab.[57] The solution for an infinite medium with a point source is

$$g_1(\tau) = \exp\left\{ -[3\mu_a l^* + k_o^{\,2} \langle \Delta r^2(\tau) \rangle]^{1/2} \frac{|\mathbf{r} - \mathbf{r}_s|}{l^*} \right\}, \tag{9}$$

where $\mathbf{r}$ is the position of the detector and $\mathbf{r}_s$ is the position of the source. With no photon absorption, the correlation function still decays as a single exponential but as $\sqrt{\langle \Delta r^2(\tau) \rangle}$ instead of $\langle \Delta r^2(\tau) \rangle$, as in the case of single scattering. Photon absorption reduces the contribution of long-path-length photons and thus suppresses the decay at early correlation times. $g_1(\tau)$ has been verified experimentally by many, including the authors of Refs. 57–59.

Similar equations for the field correlation function arising from multiply scattering systems have been obtained by means of field theory. For discussions on the derivation with field theory, see Stephen,[60] MacKintosh and John,[33] Maret and Wolf,[34] Val'kov and Romanov,[35] and Stark *et al.* in this feature.

The derivation of Eq. (8) is based on the assumptions that the successive scattering events and neighboring particle motions are uncorrelated, that the photons have scattered many times, and that the correlation time is much smaller than the time that it takes a particle to move a wavelength of light. DWS has proved to be a highly successful model for uniform, highly concentrated systems but presents difficulties when one is trying to quantify the signals from nonuniform systems.

C. Correlation Transport and Correlation Diffusion

A different approach for finding $g_1(\tau)$ that does not rely on the assumptions made in DWS has been proposed by Ackerson *et al.*[61,62] This new approach treats the transport of correlation through a scattering system much like the radiative transport equation[63,64] treats the transport of photons. The difference between the correlation transport equation (CT) and the radiative transport equation (RT) is that the CT accumulates the decay of the correlation function for each scattering event. Since contributions to the decay of the correlation function arise from each scattering event from a moving particle, one simply constructs the CT by adding the single-scattering correlation function to the term that accounts for photon scattering in the RT. This term accounts for all the scattering events. The CT is thus[61,62]

$$\nabla \cdot G_1^T(\mathbf{r}, \hat{\Omega}, \tau)\hat{\Omega} + \mu_t G_1^T(\mathbf{r}, \hat{\Omega}, \tau)$$

$$= \mu_s \int G_1^T(\mathbf{r}, \hat{\Omega}', \tau) g_1^s(\hat{\Omega}, \hat{\Omega}', \tau) f(\hat{\Omega}, \hat{\Omega}') d\hat{\Omega}'$$

$$+ S(\mathbf{r}, \hat{\Omega}). \tag{10}$$

Here $G_1^T(\mathbf{r}, \hat{\Omega}, \tau)$ is the unnormalized temporal field correlation function, which is a function of position $\mathbf{r}$, direction $\hat{\Omega}$, and correlation time τ. The scattering and the absorption coefficients are μ_s and μ_a, respectively, and $\mu_t = \mu_s + \mu_a$. $g_1^s(\hat{\Omega}, \hat{\Omega}', \tau)$ is the normalized temporal field correlation function for single scattering [see Eq. (6)]. $f(\hat{\Omega}, \hat{\Omega}')$ is the normalized differential scattering cross section. $S(\mathbf{r}, \hat{\Omega})$ is the light-source distribution. The scattering coefficient is the reciprocal of the scattering length, $\mu_s = 1/l$, and the absorption coefficient is the reciprocal of the absorption length, $\mu_a = 1/l_a$. The time dependence (not to be confused with correlation time) has been left out of the equation since we consider only measurements with cw sources and systems in equilibrium (i.e., steady state). We can include the time dependence by adding a time derivative of $G_1^T(\mathbf{r}, \hat{\Omega}, \tau)$ [i.e., $v^{-1}(\partial/\partial t)G_1^T(\mathbf{r}, \hat{\Omega}, \tau, t)$] to the left-hand side of Eq. (10) and by letting $G_1^T(\mathbf{r}, \hat{\Omega}, \tau) \rightarrow G_1^T(\mathbf{r}, \hat{\Omega}, \tau, t)$.

At zero correlation time, $\tau = 0$, there has been no decorrelation of the speckle field and the CT reduces to the RT. This equivalence arises because the unnormalized field correlation function at $\tau = 0$ is just the ensemble-averaged intensity, which is the quantity determined by the RT.

The CT provides a means for considering the intermediate regime between single-scattering systems and systems through which light diffuses. Furthermore, in the limit of single scattering, it reduces to the standard single-scattering correlation function discussed in Subsection 2.A, and, as we discuss below, solutions in the photon-diffusion regime are the same as obtained from DWS (see Subsection 2.B). The CT is useful because its validity ranges from single-scattering to multiple-scattering systems and because it affords a straightforward approach to considering systems with spatially varying optical and dynamical properties. A drawback to the CT is the difficulty in obtaining analytical and numerical solutions. The RT is plagued by the same problem. Because of the similarity between the CT and the RT we should be able to apply the same approximation methods to the CT as we applied to the RT.

Using the standard diffusion approximation, we may reduce the CT to the correlation diffusion equation (see Appendix A):

$$[D_\gamma \nabla^2 - v\mu_a - {}^1\!/{}_3\, v\mu_s' k_o^{\,2} \langle \Delta r^2(\tau) \rangle] G_1(\mathbf{r}, \tau) = -vS(\mathbf{r}). \tag{11}$$

Here $D_\gamma = v/(3\mu_s')$ is the photon-diffusion coefficient, v is the speed of light in the medium, and $\mu_s' = \mu_s(1 - \langle \cos\theta \rangle) = 1/l^*$ is the reduced scattering coefficient, where $\langle \cos\theta \rangle$ is the average cosine of the scattering angle. Recall that for Brownian motion $\langle \Delta r^2(\tau) \rangle = 6D_B\tau$ and for random flow $\langle \Delta r^2(\tau) \rangle = \langle \Delta V^2 \rangle \tau^2$.

To obtain the correlation diffusion equation it is necessary to assume that the photons are diffusing, that the scattering phase function $[f(\hat{\Omega}, \hat{\Omega}')]$ and the single-scattering correlation function $[g_1^s(\hat{\Omega}, \hat{\Omega}', \tau)]$ depend only on the scattering angle $\hat{\Omega} \cdot \hat{\Omega}'$, and that $k_o^{\,2} \langle \Delta r^2(\tau) \rangle \ll 1$. The photon-diffusion assumption is valid if the photon random-walk step length is smaller than the dimensions of the sample and the photon absorption length. The scattering angle assumption (i.e.,

$\hat{\Omega} \cdot \hat{\Omega}'$) is valid for systems with randomly oriented scatterers and isotropic dynamics (e.g., Brownian motion and random flow). The short-time assumption requires the correlation time τ to be much smaller than the time that it takes a scatterer to move a wavelength of light. When the photon wavelength is 514 nm and the dynamics are Brownian motion with $D_B = 1 \times 10^{-8}$ cm^2 s^{-1}, then the short-time assumption requires that $\tau \ll 1 \times 10^{-3}$ s. The breakdown of this approximation is explored in Section 5.

Equation (11) can be recast as a Helmholtz equation for the field correlation function, i.e.,

$$[\nabla^2 + K^2(\tau)]G_1(\mathbf{r}, \tau) = -\frac{vS}{D_\gamma}\delta^3(\mathbf{r} - \mathbf{r}_s), \quad (12)$$

where $K^2(\tau) = v[\mu_a + \frac{1}{3}\mu_3' k_o^2 \langle \Delta r^2(\tau)\rangle]/D_\gamma$. Here we have taken the light source to be pointlike, i.e., cw, and located at position $\mathbf{r}_s$. Note that $\frac{1}{3}\mu_s' k_o^2 \langle \Delta r^2(\tau)\rangle$ is a loss term similar to μ_a. Whereas μ_a represents losses due to photon absorption, $\frac{1}{3}\mu_s' k_o^2 \langle \Delta r^2(\tau)\rangle$ represents the absorption of correlation due to dynamic processes. When $\tau = 0$ there is no dynamic absorption, and Eq. (12) reduces to the steady-state photon-diffusion equation.

For an infinite, homogeneous system the solution to Eq. (12) has the well-known form

$G_1(\mathbf{r}, \tau)$

$$= \frac{vS \exp\left\{-[3\mu_a l^* + k_o^2 \langle \Delta r^2(\tau)\rangle]^{1/2} \frac{|\mathbf{r} - \mathbf{r}_s|}{l^*}\right\}}{4\pi D_\gamma |\mathbf{r} - \mathbf{r}_s|}. \quad (13)$$

This same solution has been derived within the context of DWS[32,34] [see Eq. (9)] and from the scalar wave equation for the electric field propagating in a medium with a fluctuating dielectric constant.[33,60] In contrast to these two approaches, the correlation diffusion equation provides a simple framework for considering turbid media with large-scale spatially varying dynamics and optical properties.

With some difficulty, such systems can be considered with DWS. We have considered this possibility and have found that DWS generally requires the computation of complicated integrations of photon dwell times in localized volume elements (voxels) convolved with a volume integral. By contrast, the correlation diffusion equation requires only the solution of a simple differential equation. Because the correlation diffusion equation is analogous to the photon-diffusion equation, we can apply all the techniques developed in the photon migration community[1–4] and elsewhere[65,66] to correlation diffusion. In the next few sections we demonstrate the scattering of correlation from dynamical inhomogeneities as well as tomographic reconstructions of the spatially varying dynamical properties of turbid media.

D. Ergodicity

The samples that we study experimentally are not always ergodic; that is, the time-averaged measurements are not equivalent to the ensemble average computed by the various photon correlation spectroscopy theories. This situation arises whenever the sample has static and dynamic scattering components, and it presents a problem when one is measuring the temporal intensity correlation function $g_2(\tau)$. It is not a problem if one is directly measuring the temporal field correlation function $g_1(\tau)$. To understand the origin of the problem, it is necessary to consider the electric field emerging from a nonergodic system and to derive $g_1(\tau)$ and $g_2(\tau)$.[67–70] We briefly outline the important experimental considerations.

The following discussion assumes that the sample is highly scattering and comprises two components: a static, nonergodic component; and a dynamic, ergodic component. The electric field reaching the detector is a superposition of photons that have migrated through the static region without scattering from moving particles and photons that have scattered at least once from a moving (dynamic) particle. We refer to these two different types of photons as constant and fluctuating. Thus

$$\mathbf{E}(t) = \mathbf{E}_c(t) + \mathbf{E}_f(t). \quad (14)$$

With these definitions the temporal intensity correlation function is found to be[39,67–70]

$$g_2(\tau) = 1 + \frac{2\sqrt{\beta}I_c \langle I_f\rangle |g_{1,f}(\tau)| + \beta\langle I_f\rangle^2 |g_{1,f}(\tau)|^2}{(I_c + \langle I_f\rangle)^2}. \quad (15)$$

Here $\langle\ \rangle$ denotes a time average. $\mathbf{E}_c$ does not fluctuate in time, and thus the intensity $I_c = \langle \mathbf{E}_c(t)\mathbf{E}_c^*(t + \tau)\rangle$ is constant. $\mathbf{E}_f(t)$ does fluctuate in time, so that $\langle I_f\rangle = \langle \mathbf{E}_f(t)\mathbf{E}_f^*(t)\rangle$ is the time-averaged fluctuating intensity and $g_{1,f}(\tau)$ is the temporal field correlation function of $\mathbf{E}_f(t)$ (this decays from 1 to 0). $g_2(\tau)$ presented in Eq. (15) has a heterodyne term, $2I_c\langle I_f\rangle|g_{1,f}(\tau)|$, and a homodyne term, $\langle I_f\rangle^2|g_{1,f}(\tau)|^2$. We have included the coherence factor β, which depends on the number of speckles averaged and on the laser coherence length. When one is measuring a single speckle created by a stable, long-coherence-length laser, then $\beta = 1$. Unfortunately, experimentally, β usually varies between 0 and 1 and must be measured. It is safe to assume that β will remain constant for measurements made on different speckles, since β depends only on the laser and detection optics. However, I_c will vary, changing the relative importance of the homodyne and the heterodyne terms.

There are a few methods for circumventing this problem.[67–70] To obtain the proper correlation function we ensemble average during the acquisition of the intensity correlation function. This method was described in detail by Xue et al.[67] The technique for ensemble averaging that we used is explained in Section 3. Basically, the idea is to move the detector from speckle to speckle during the course of the measurement. In this way, $\mathbf{E}_c(t)$ will fluctuate on a time scale given by the motion of the detector from speckle to speckle. The normalized intensity correlation function is thus

$$g_2(\tau) = 1 + \beta \frac{[\langle I_c\rangle |g_{1,c}(\tau)| + \langle I_f\rangle |g_{1,f}(\tau)|]^2}{(\langle I_c\rangle + \langle I_f\rangle)^2}. \quad (16)$$

$g_{1,c}(\tau)$ is the field correlation function of the fluctuating $\mathbf{E}_c(t)$ and decays in a log-linear fashion on a time scale that is proportional to the amount of time that it takes to

move the detector from one speckle to the next.[68] If the detector speed is sufficiently slow that the decay time of $g_{1,c}(\tau)$ is much longer than that of $g_{1,f}(\tau)$, then the measured correlation function will look like that shown in Fig. 3, and the fluctuations due to sample dynamics are easily separated from ensemble-averaging fluctuations. The correlation function at early times when $g_{1,c}(\tau) \approx 1$ is then

$$g_2(\tau) = 1 + \beta \frac{[\langle I_c \rangle + \langle I_f \rangle |g_{1,f}(\tau)|]^2}{(I_c + \langle I_f \rangle)^2}, \qquad (17)$$

and from the Siegert relation[32,34,37] we find that

$$g_1(\tau) = \frac{[\langle I_c \rangle + \langle I_f \rangle |g_{1,f}(\tau)|]}{(\langle I_c \rangle + \langle I_f \rangle)}. \qquad (18)$$

This is exactly the temporal field correlation function that we calculate with the correlation diffusion theory. There is no need to separate $\langle I_f \rangle |g_{1,f}(\tau)|$ from $\langle I_c \rangle$. From the plateau in the correlation function that occurs when $g_{1,f}(\tau) \ll 1$ it is possible to determine $\langle I_c \rangle$ and thus $\langle I_f \rangle$ and $|g_{1,f}(\tau)|$. However, for comparisons with solutions of the correlation diffusion equation it is not necessary to make this separation; it is only necessary that $g_{1,c}(\tau) \approx 1$ for the temporal region of interest.
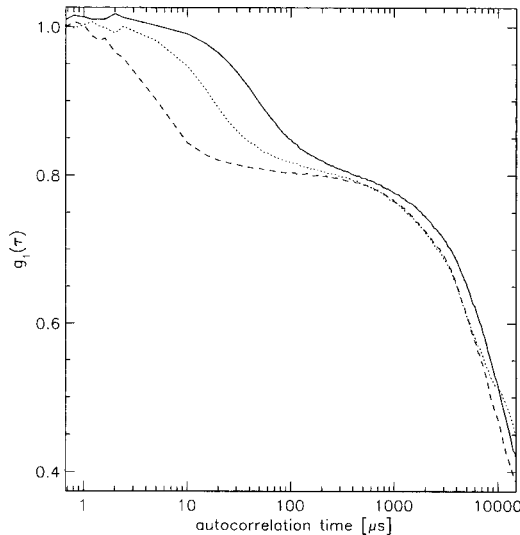

Fig. 3. Ensemble-average correlation function from a nonergodic turbid medium. The medium is a solid, highly scattering slab with a cylindrical vein through which a highly scattering colloid flows. The early τ decay corresponds to the flow dynamics, whereas the long τ decay results from the ensemble averaging. The three curves come from three different flow speeds, with the solid, the dotted, and the dashed curves corresponding to flow speeds of 0.08, 0.24, and 0.88 cm s^{-1}, respectively. The early τ decay rate increases with the flow speed. The longer τ decay depends only on the rate of ensemble averaging, which is held constant. The intermediate plateau reveals the relative magnitudes of $\langle I_c \rangle$ and $\langle I_f \rangle$ and tells us what fraction of the detected photons have sampled the dynamic region. Here $\langle I_c \rangle/(\langle I_c \rangle + \langle I_c \rangle) \approx 0.8$, which reveals that 80% of the photons have not sampled the dynamic region. This is independent of the flow speed, as expected.

3. EXPERIMENTAL SETUP

Photons scattered by moving particles have their frequency Doppler shifted by an amount proportional to the particle's speed, the photon's wave number, and the scattering angle. The frequency shifts are generally a very small fraction of the absolute frequency, typically ranging from 10^{-9} to 10^{-12}. These relatively small shifts are difficult to measure directly with, for example, spectral filters such as a Fabry–Perot filter. Instead we usually determine them indirectly by measuring the beating of different frequencies as revealed in the fluctuating intensities of a single coherence area (i.e., speckle) of the scattered light. We analyze these fluctuations by looking at the power spectrum or the temporal autocorrelation function of the fluctuations. We measure the temporal intensity autocorrelation function of the fluctuating speckles. This method is sometimes preferred over measuring the power spectrum, since digital correlators and photon-counting techniques make it possible to analyze smaller signals.

There is one major advantage of direct measurements of the spectrum. Indirect measurements of the Doppler broadening of the laser linewidth require that single (or only a few) coherence areas of scattered light be detected. For systems that multiply scatter light, these coherence areas are of the order of ~ 1 μm^2. Small-aperture light collectors are thus necessary, resulting in the collection of small numbers of photons. This is not the case for systems that scatter light no more than once, since the coherence area is then given by the laser-beam size and coherence length. For direct measurements of Doppler broadening it is not necessary to collect light from a single coherence area, and thus the number of photons collected can be increased.

A. Experimental Methods

A schematic of the experimental apparatus for measuring the temporal intensity autocorrelation function of a speckle's intensity fluctuations is presented in Fig. 4. For the initial experiments, the 514-nm line of an Ar-ion laser (operating with an étalon) is used because of its long coherence length and strong power. For the animal experiments, the 632-nm line of a He–Ne laser is used because of its portability. In the future it will be desirable to utilize laser diodes with stable, single-longitudinal-mode operation.

The laser beam is coupled into a multimode fiber. Fibers with core diameters ranging from 50 to 200 μm and various numerical apertures (NA's) are used. Generally, for large source–detector separations the diameter and the NA are not critical, although coupling with the laser beam is easier with large diameters and large NA's. For the smaller source–detector separations used on the human subject and animal trials, it is best to use a small NA. This minimizes the divergence of the beam from the output of the fiber to the sample, thus reducing the possibility of detecting light that has reflected at the surface of the sample. For these measurements we use 200-μm core-diameter fiber with a NA of 0.16.

Measurements are made on various samples with many source–detector separations. The source–detector
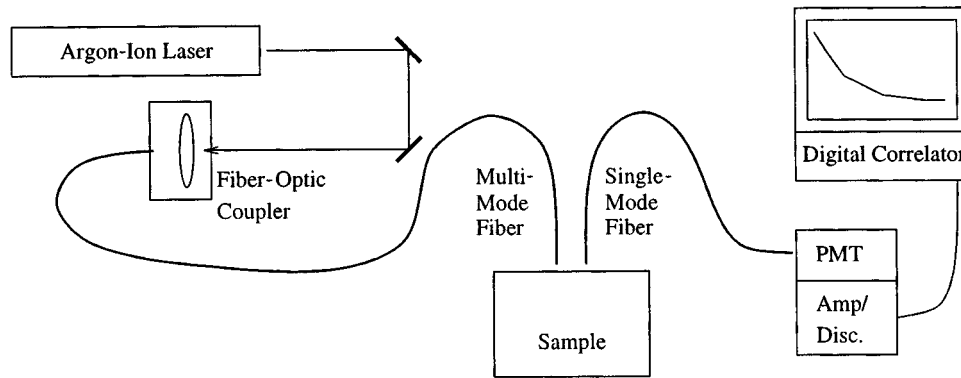
Fig. 4.   Experimental setup for photon correlation spectroscopy. Amp/Disc., amplifier–discriminator.

positions are controlled by repositioning of the source and the detector fibers. Diffuse back reflection is measured from turbid, homogeneous, and solid slabs with either a spherical cavity containing a turbid colloid or a cylindrical vein through which a colloid is pumped. Transmission and reflection measurements are made on solid cylinders with spherical cavities. Animal subjects are also employed. These various samples are described in more detail below in the relevant sections.

Single speckles of the diffuse light emanating from the sample are collected with a single-mode fiber. A single-mode fiber does not actually collect light from a single speckle but projects the collected light into a single spatial mode (actually, the single-mode fiber propagates both polarizations, so it is really a dual-mode fiber).[71–73] The collected light is delivered to a photon-counting photomultiplier tube (PMT; Hamamatsu, Corp., Model HC120). The dark count is less than 10 counts/s at room temperature. Smaller dark counts are achieved by cooling of the PMT to 0 °C. After-pulsing can occur for up to 100 ns, and the response of the PMT–amplifier–discriminator system is linear up to 200,000 counts/s. The signal from the PMT is amplified and is then discriminated and fed to the digital correlator card housed in a 486 computer. To measure correlation functions faster than 200 ns it is necessary to cross correlate the signal from two PMT's. This is best achieved by use of a 50–50 fiber-optic beam divider to split the beam between two PMT's and operate the digital correlator in cross-correlation mode.

The samples used in our experiments are nonergodic (a time average is not equal to an ensemble average). As described in the theory section on photon correlation spectroscopy and ergodicity (Subsection 2.D), care must be taken with nonergodic samples to obtain repeatable measurements. Basically, for nonergodic samples each speckle has a constant component and a fluctuating component. The constant component consists of photons that have not scattered from any moving particles. The fluctuating component arises from the photons that have scattered from at least one moving particle. If we fix the source and compare speckles in a localized region some distance from the source, then we will see that the fluctuating component is the same from speckle to speckle (the ensemble average equals the time average) but that the constant component differs (the ensemble average does

not equal the time average). This variation in the constant component causes the measured temporal intensity correlation function to vary from speckle to speckle.

To measure the proper correlation function it is necessary to ensemble average the signal. We do this by moving the sample (or sometimes the source and the detector) during the integration of a correlation function. In this way we measure an ensemble of constant components and thus obtain the desired ensemble average of the speckles' intensity. Moving the sample affects the correlation function by increasing the observed intensity fluctuation. If the motion is slow enough, then the decay of the correlation function due to moving the sample occurs on a time scale that is long compared with the time scale of interest. However, if we move the sample too fast, then the ensemble-averaging decay overlaps with the decay due to the internal dynamics.

A schematic of the system that we use for moving the sample is shown in Fig. 5. The sample is placed on a translation stage that is driven by a servomotor. It is important to use a motor that moves smoothly. Stepper motors do not work well because their motion is jerky. This jerky motion results in fast intensity fluctuations that obscure the intensity fluctuations that are due to the internal dynamics. The speed of the servomotor is set to move the sample approximately 50 μm s^{-1}. It is important to ensemble average the signal in a localized area. If we average over too large an area, then source–detector positions relative to objects in the sample are not well defined, and accurate comparisons with theory cannot be made. We use limit switches on the servomotor to make it oscillate on a 400-μm path.

B. Monte Carlo Simulations
When the accuracy of our experimental results were questionable or when we did not have the experimental data, we used the results from Monte Carlo simulations to check the accuracy of the correlation diffusion equation and its solutions (see Section 5). In many cases these simulations provide a signal-to-noise ratio that is difficult to achieve in the laboratory and therefore permit a more accurate test of the validity of the correlation diffusion theory. We ran simulations for a point source in an infinite medium. Media with different dynamical properties

were considered. First, we gathered data for a system with spatially uniform Brownian motion. The correlation diffusion equation is known to be valid for this system at short correlation times. Therefore these first simulations worked as a test for the Monte Carlo code at early correlation times and to demonstrate the breakdown of the diffusion equation at long correlation times.

Next, we ran simulations for a homogeneous solid system containing a spherical region with scatterers undergoing Brownian motion. These simulations are necessary to unravel systematic discrepancies between experimental data and correlation diffusion theory.

Finally, simulations were executed for a homogeneous system with different volume fractions of random flow. This is a model of tissue blood flow. All the simulations were performed assuming isotropic scattering (i.e., $g = 0$).

The theoretical details pertinent to the Monte Carlo simulation are reviewed here. A complete discussion of deriving temporal electric-field correlation functions $[g_1(\tau)]$ was given in Section 2. The correlation function of light that scatters once from a dilute suspension of noninteracting uncorrelated particles is

$$g_1{}^s(\tau) = \exp[-{}^1\!/{}_6 q^2 \langle \Delta r^2(\tau) \rangle], \qquad (19)$$

where $\mathbf{q} = \mathbf{k}_{\mathrm{out}} - \mathbf{k}_{\mathrm{in}}$ is the momentum transfer imparted by the scattering event (see Fig. 1) and $\langle \Delta r^2(\tau) \rangle$ is the mean-square displacement of the scattering particles in time τ. The magnitude of the momentum transfer is $q = 2k_o \sin(\theta/2)$. When photons are multiply scattered by noninteracting uncorrelated particles, the correlation function is computed for a given photon path α with n uncorrelated scattering events as

$$g_1{}^{(\alpha)}(\tau) = \exp\left[-\frac{1}{6} \sum_{j=1}^{n} q_{\alpha,j}{}^2 \langle \Delta r^2(\tau) \rangle \right]. \qquad (20)$$

$q_{\alpha,j}$ is the momentum transfer experienced along path α at scattering site j.

The general procedure for considering multiple paths is to first relate the total dimensionless momentum transfer $Y = \Sigma_{j=1}^{n} q_{\alpha,j}{}^2 / 2k_o{}^2 = \Sigma_{j=1}^{n}(1 - \cos \theta_{\alpha,j})$ to the dimensionless path length $S = s/l^*$. Here s is the length of the photon trajectory through the sample and l^* is the photon random-walk step length. For large n, Y is accurately approximated by the average over the scattering form factor, and thus

$$Y \approx n\langle 1 - \cos \theta \rangle = \frac{nl}{l^*} = \frac{s}{l^*} = S. \qquad (21)$$
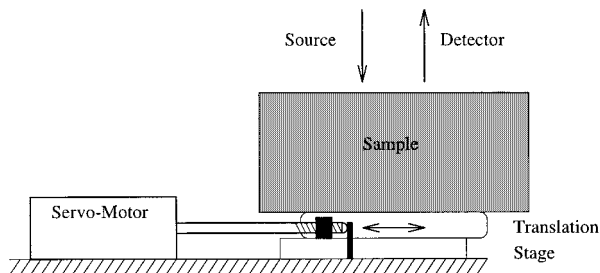

Fig. 5. Setup for performing the ensemble average.

Here $\langle\ \rangle$ denotes the average over the scattering form factor and l is the photon scattering length that equals the photon random-walk step length when the scattering is isotropic. Next the total correlation function is obtained from the weighted average of Eq. (20) over the distribution of path lengths, i.e.,

$$g_1(\tau) = \int_0^\infty P(S) \exp[k_o{}^2 \langle \Delta r^2(\tau) \rangle S/3] \mathrm{d}S. \qquad (22)$$

Although $P(S)$ can be determined by Monte Carlo simulations, it is usually found with the help of the photon-diffusion equation.

This procedure has built into it two assumptions: the relation between Y and S, and the assumption that $P(S)$ is accurately given by the photon-diffusion equation. For the purposes of the Monte Carlo simulations it is desirable to take a different approach that does not make these two assumptions. As suggested by Middleton and Fisher,[74] and by Durian,[75] the total correlation function can be obtained from a weighted average over the total dimensionless momentum transfer experienced by all the photon trajectories, i.e.,

$$g_1(\tau) = \int_0^\infty P(Y) \exp\left[\frac{1}{3} Y k_o{}^2 \langle \Delta r^2(\tau) \rangle \right] \mathrm{d}Y. \qquad (23)$$

There are no assumptions in this formulation other than the standard noninteracting uncorrelated particles assumption. The drawback is that $P(Y)$ cannot be calculated analytically. However, Monte Carlo simulations provide a simple numerical approach to finding $P(Y)$ for different geometries. Such Monte Carlo simulations are described by Middleton and Fisher,[74] by Durian,[75] and by Koelink et al.[76]

The Monte Carlo simulation follows the trajectory of a photon, using the algorithm described below, with the addition that the dimensionless momentum transfer Y is incremented in dynamic regions. When the photon reaches a detector, the Y associated with that photon is scored in a $P(Y)$ histogram. After enough statistics have been accumulated for $P(Y)$ (typically 1 million to 10 million photons), $g_1(\tau)$ can be calculated with Eq. (23).

The basic idea of the Monte Carlo algorithm is to launch N photons into the medium and to obtain a histogram of partial photon flux in radial and momentum-transfer channels. For our simulations N is typically 1 million to 10 million, and the code takes ~2 h to run on a Sun SPARC 10 Model 512 50-MHz processor or a 75-MHz Pentium.

There are many techniques for propagating and obtaining histograms of photons within Monte Carlo calculations.[77–79] To keep the code simple we mimic the physical process as closely as possible instead of relying on reduction techniques that purport to increase statistics while reducing computation (see Refs. 77–79 for discussions of different reduction techniques). To propagate a photon from one interaction event to the next, the program calculates a scattering length and an absorption length based on the exponential distributions derived from the scattering and the absorption coefficients, respectively. If the absorption length is shorter than the scattering length, then the photon is propagated the ab-

sorption length, scored if necessary, and terminated, and a new photon is launched from the source position. If the scattering length is shorter, then the photon is propagated the scattering length, scored if necessary, and the scattering angle is calculated based on the commonly used Henyey–Greenstein phase function,[78–80] and then a new scattering length and absorption length are calculated. Photon propagation continues until the photon is absorbed or escapes, or until the time exceeds a maximum set by T_{gate} (typically 10 ns).

To exploit the spherical symmetry of the problem for infinite homogeneous media (the source is isotropic), spherical shell detectors are centered on the point source, and the crossing of photons across each shell is scored in the appropriate momentum-transfer and radial channels. Inward and outward crossings are scored separately so that the Monte Carlo simulation can report the radial components of the correlation flux. In this way we can obtain the correlation fluence, $\Phi(r)$, and the net correlation flux, $-D\nabla\Phi(r)$, from the data. For our analyses we use the correlation fluence.

For problems with cylindrical symmetry, e.g., semi-infinite media and a spherical inhomogeneity with the source on the z axis, circular ring detectors were used. These ring detectors were contained in an xy plane and were 2 mm wide. Photons were scored as they crossed the rings in positive and negative z directions.

4. EXPERIMENTAL RESULTS

In this section we measure the correlation function on turbid media with spatially varying dynamics and optical properties. We compare these measurements with predictions from correlation diffusion theory to demonstrate the accuracy of the correlation diffusion equation, and we demonstrate that images of spatially varying dynamics can be reconstructed. We first check the validity of the model for systems with a spherical heterogeneity characterized by a different Brownian diffusion coefficient and optical properties (Subsection 4.A). Subsection 4.B demonstrates an image reconstruction of a system with spatially varying Brownian motion. Subsection 4.C verifies the theory's validity for systems with spatially varying flow. In Subsection 4.D we show that the correlation diffusion equation can accurately quantify the thickness of a layered structure characterized by different dynamical properties. Burned tissue is essentially a layered structure. This last result therefore suggests that correlation diffusion spectroscopy can be used to quantify tissue burn depth, as is explored on a pig model in Section 6.

A. Validity of Diffusion Equation for Media with Spatially Varying Brownian Motion

Here we compare experimental and theoretical results to verify the validity of the correlation diffusion equation for turbid media with spatially varying dynamical and optical properties. The first experiments that we describe are performed on a turbid slab that is static and homogeneous except for a spherical region, which is dynamic. Dynamic regions with different magnitudes of Brownian motion and different scattering coefficients are considered.

Before discussing the experiment, we briefly review the solution to Eq. (11) for a medium that is homogeneous except for a spherical region (with radius a) characterized by optical and dynamical properties different from those of the surrounding medium. The spherical region can also be characterized by different optical properties. The analytic solution of the correlation diffusion equation for this system reveals that the measured correlation function outside the sphere can be interpreted as a superposition of the incident correlation function plus a term that accounts for the scattering of the correlation from the sphere, i.e.,
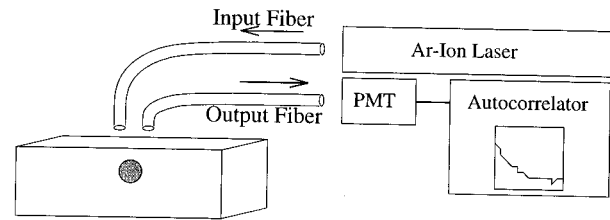

Fig. 6. Setup of an experiment in which a 514-nm line from an Ar-ion laser (operated at 2.0 W with an étalon) is coupled into a multimode fiber-optic cable and is delivered to the surface of a solid slab of TiO_2 suspended in resin. The slab has dimensions of $15 \times 15 \times 8$ cm. A spherical cavity with a diameter of 2.5 cm is located 1.8 cm below the center of the upper surface. The cavity is filled with a 0.2% suspension of 0.296-μm-diameter polystyrene spheres at 25 °C, resulting in $\mu_s' = 6.67$ cm^{-1}, $\mu_a' = 0.002$ cm^{-1}, and $D_B = 1.5 \times 10^{-8}$ cm^2 s^{-1}. For the solid slab, $\mu_s' = 4.55$ cm^{-1} and $\mu_a = 0.002$ cm^{-1}. A single-mode fiber collects light at a known position and delivers it to a PMT whose output enters a digital autocorrelator to obtain the temporal intensity correlation function. The temporal intensity correlation function is related to the temporal field correlation function by the Siegert relation.[32,34,37] The fibers can be moved to any position on the sample surface.
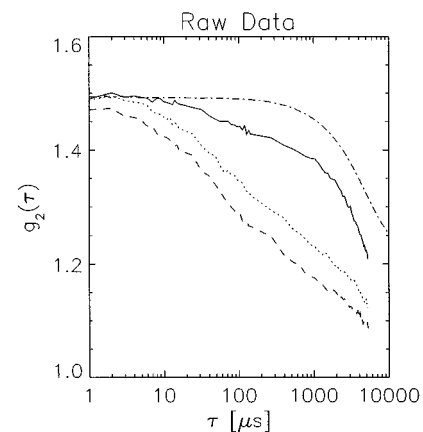

Fig. 7. Experimental measurements of the temporal intensity autocorrelation function for three different source–detector pairs with a colloid present and one source–detector position without the colloid. The dotted–dashed curve illustrates the correlation function decay that is due to ensemble averaging (i.e., no colloid is present in the spherical cavity). This decay is independent of the source–detector position. The dashed, dotted, and solid curves correspond to $g_2(\tau)$ measured with a colloid in the cavity and the source–detector positions at 1, 2, and 3, respectively, as indicated in Fig. 8.
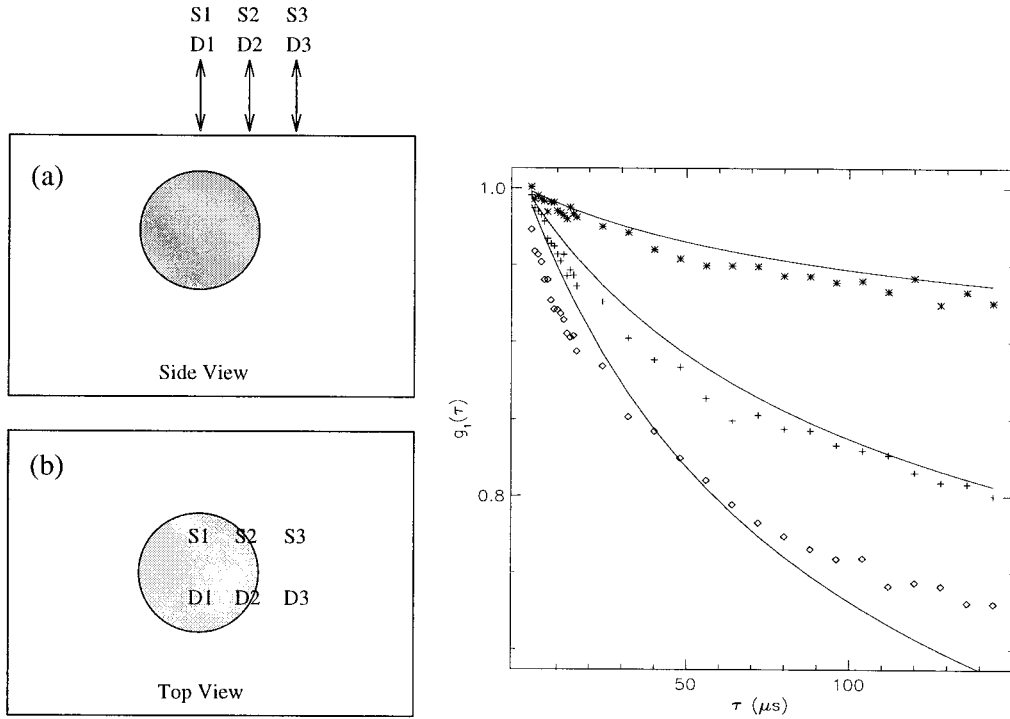
Fig. 8. Experimental measurements of the normalized temporal field autocorrelation function for three different source–detector pairs in comparison with theory. The geometry is illustrated in (a) and (b). With respect to an x–y coordinate system whose origin lies directly above the center of the spherical cavity, the source–detector axis was aligned parallel to the y axis with the source at $y = 1.0$ cm and the detector at $y = -0.75$ cm. Keeping the source–detector separation fixed at 1.75 cm, we made measurements at $x = 0.0, 1.0, 2.0$ cm, indicated by the symbols $\diamond$, $+$, and $*$, respectively. The uncertainty for these measurements is 3% and arises from uncertainty in the position of the source and the detector. The curves were calculated with the known experimental parameters, with D_B being a free parameter (see Fig. 6). Note that larger and more rapid decays are observed when the source and the detector are nearest the dynamic sphere.

$$G_1^{\text{out}}(\mathbf{r}_s, \mathbf{r}_d, \tau) = \frac{S \, \exp[iK^{\text{out}}(\tau)|\mathbf{r}_d - \mathbf{r}_s|]}{4\pi D_\gamma |\mathbf{r}_d - \mathbf{r}_s|} + \sum_{l=0}^{\infty} A_l h_l^{(1)}$$
$$\times [K^{\text{out}}(\tau)r_d][K^{\text{out}}(\tau)\mathbf{r}_d] Y_l^0(\theta, \phi).$$

(24)

Here $h_l^{(1)}$ are Hankel functions of the first kind and $Y_l^0(\theta, \phi)$ are spherical harmonics. The sphere is centered on the origin, and the source is placed on the z axis to exploit azimuthal symmetry. The coefficient A_l is the scattering amplitude of the lth partial wave and is found by application of the appropriate boundary conditions on the surface of the sphere. The boundary conditions are similar to that for the photon-diffusion equation.[81,82] Specifically, the diffuse correlation must be continuous across the boundary, and the net flux must be normal to the boundary, i.e., $G_1^{\text{out}}(a, \tau) = G_1^{\text{in}}(a, \tau)$ and $-D_\gamma^{\text{out}}\hat{r} \cdot \nabla G_1^{\text{out}}(\mathbf{r}, \tau)|_{r=a} = -D_\gamma^{\text{in}}\hat{r} \cdot \nabla G_1^{\text{in}}(\mathbf{r}, \tau)|_{r=a}$ on the surface of the sphere. $G_1^{\text{in}}(\mathbf{r}, \tau)$ is the correlation function inside the spherical object, and $\hat{r}$ is the normal vector to the sphere. Applying these boundary conditions, we find that

$$A_l = \frac{-ivSK^{\text{out}}}{D_\gamma^{\text{out}}} h_l^{(1)}(K^{\text{out}}z_s) Y_l^{0*}(\pi, 0)$$
$$\times \left[\frac{D_\gamma^{\text{out}}xj_l'(x)j_l(y) - D_\gamma^{\text{in}}yj_l(x)j_l'(y)}{D_\gamma^{\text{out}}xh_l^{(1)'}(x)j_l(y) - D_\gamma^{\text{in}}yh_l^{(1)}(x)j_l'(y)} \right], \quad (25)$$

where j_l are the spherical Bessel functions of the first kind, $x = K^{\text{out}}a$, $y = K^{\text{in}}a$, a is the radius of the sphere, $\mathbf{r}_s$ is the position of the source, and j_l' and $h_l^{(1)'}$ are the first derivatives of the functions j_l and $h_l^{(1)}$ with respect to the argument. This solution has been discussed in detail for diffuse photon-density waves.[81,82]

We demonstrate the scattering of temporal correlation by a dynamical inhomogeneity in an experiment shown in Fig. 6. In this experiment the temporal intensity correlation function is measured in remission from a semi-infinite, highly scattering, solid slab of TiO_2 suspended in resin ($D_B = 0$). The slab contains a spherical cavity filled with a turbid, fluctuating suspension of 0.296-μm polystyrene microspheres ($D_B = 1.5 \times 10^{-8}$ cm^2 s^{-1}). The measured temporal intensity correlation function, $g_2(\tau)$, for three different source–detector separations is presented in Fig. 7. $g_2(\tau)$ is plotted for the system with no Brownian motion (i.e., no colloid is present) to illustrate the time scale of the decay introduced by ensemble averaging. From the raw data we can see that $\beta \approx 0.5$, as expected, since we are using a single-mode fiber that propagates the two orthogonal polarizations. We also observe the short-time decay of the correlation function, which is due to Brownian motion, and the long-time decay due to ensemble averaging. The decay due to ensemble averaging is significant for $\tau > 300$ μs and is not dependent on source–detector position or separation. We focus on the decay for $\tau < 200$ μs.

Figure 8 exhibits the decay of the normalized temporal field correlation function, $g_1(\tau)$, obtained from $g_2(\tau)$ with the Siegert relation [Eq. (4)], and compares these results to theoretical predictions based on Eq. (24). The expected trend is observed. When the source and the detector are closer to the dynamical region there is more decay in the correlation function, and the rate of decay is greater. Here the largest fraction of detected photons has sampled the dynamical region and on average has had more scattering events in the dynamical region. The quantitative agreement between experiment and theory is not good; to obtain good agreement one must reduce the Brownian diffusion coefficient in the spherical region by a factor ~4. For the theoretical results presented in Fig. 8, $D_B = 3.77 \times 10^{-9}$ cm^2 s^{-1}, which is a factor of ~4
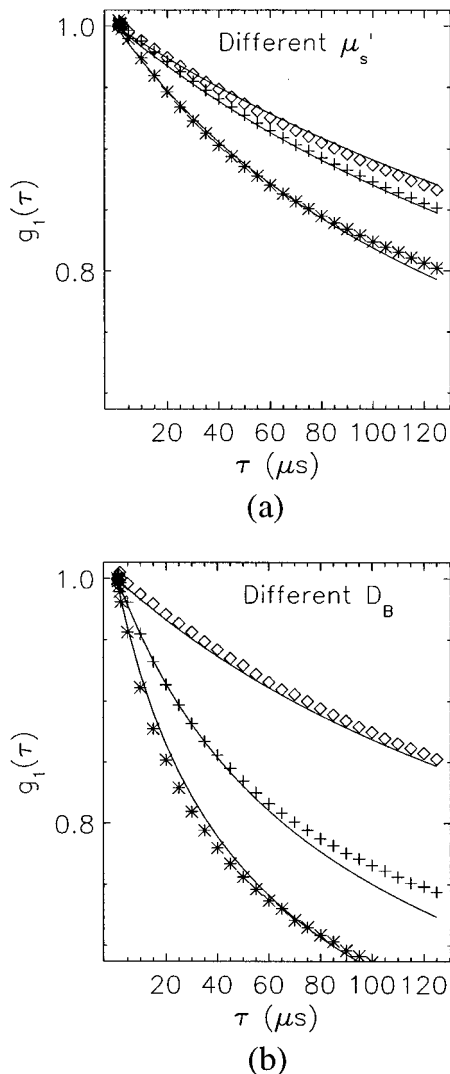

(a)

(b)

Fig. 9. Experimental measurements of the normalized field correlation function for a dynamical region (a) with three different μ_s' values plotted and (b) for three different D_B values. The source and the detector were separated by 1.5 cm and were centered over the position of the sphere. In (a) the symbols $\diamond$, +, and $*$ correspond to $\mu_s' = 3.5, 4.5, 9.0$ cm^{-1}, respectively. The curves were calculated with the known experimental parameters, with D_B being a free parameter. In (b) the symbols, $\diamond$, +, and $*$ correspond to $a = 0.813, 0.300, 0.137$ μm, respectively.

smaller than the expected $D_B = 1.5 \times 10^{-8}$ cm^2 s^{-1}. The cause of this discrepancy is discussed below.

Correlation functions were measured for different reduced scattering coefficients and Brownian diffusion coefficients for the dynamical region. Figure 9(a) plots the measured correlation functions for different μ_s' compared with theory. Three different concentrations of 0.813-μm-diameter polystyrene microspheres were used to obtain reduced scattering coefficients of 3.5, 4.5, and 9.0 cm-1 for the dynamical region. The rest of the system is the same as the previous experiment (see Fig. 6). With the Brownian diffusion coefficient as a free parameter to fit the theory to experiment, good agreement was obtained. In all the cases the Brownian diffusion coefficient had to be reduced by a factor of ~3. For 0.813-μm-diameter polystyrene microspheres the expected D_B value is 5.46 $\times$ 10^{-9} cm^{-1}. For $\mu_s' = 3.5, 4.5, 9.0$ cm^{-1} the fits for D_B were 2.21×10^{-9}, 2.14×10^{-9}, and 1.78×10^{-9} cm^2 s^{-1}, respectively.

Correlation functions for different Brownian diffusion coefficients are plotted in Fig. 9(b). Different D_B values were obtained by use of monodisperse polystyrene microspheres with diameters of 0.137; 0.300; and 0.813 μm. The concentrations were varied to keep μ_s' = 4.5 cm^{-1}. Once again, good agreement between experiment and theory was observed by use of a smaller D_B value in the theory. The relative values for the fitted D_B agree with those of the experimental D_B. The expected values of D_B were 3.28×10^{-8}, 1.50×10^{-8}, and 5.46×10^{-9} cm^2 s^{-1}, respectively, for the polystyrene microspheres with diameters of 0.137, 0.300, and 0.813 μm. The fitted values for D_B were 1.49×10^{-8}, 8.21×10^{-9}, and 2.71×10^{-9} cm^2 s^{-1}.

We believe that the observed disagreement in the Brownian diffusion coefficient results from mismatches in the indices of refraction at the resin–air and resin–colloid interfaces. In an early analysis[38] the semi-infinite boundary condition was solved incorrectly but fortuitously resulted in better agreement. In that case[38,40] the point source was not placed a distance of $l^* = 1/\mu_s'$ away from the collimated source along the source axis, as in the usual treatment of a collimated source,[83] but rather at the collimated source position. Furthermore, the image source (to satisfy the extrapolated boundary condition for index-mismatched media) was positioned as if the real source had been extended into the medium. This treatment resulted in quantitative agreement between theory and experiment.

Discrepancies between experiment and theory also arise because a significant fraction of the detected photons scatter from the dynamical region only a few times before detection, but these discrepancies are small compared with those that arise from mismatches in the indices of refraction.[39]

The high sensitivity to the treatment of the semi-infinite boundary conditions and the mismatch in the indices of refraction renders this experimental setup inappropriate for rigorously validating the correlation diffusion equation for systems with spatially varying dynamical and optical properties. In Subsection 4.B we compare the theory with Monte Carlo results for infinite media with spherical inhomogeneities and obtain quanti-

tative agreement. The agreement supports the view that correlation scatters from spatial variations of the particle diffusion coefficient [$D_B(\mathbf{r})$], the absorption [$\mu_a(\mathbf{r})$], and the reduced scattering coefficient [$\mu_s'(\mathbf{r})$].

B. Image Reconstruction in Media with Spatially Varying Brownian Motion

Since the perturbation of correlation by inhomogeneities can be viewed as a scattering process, one readily can envision the application of tomographic algorithms for the reconstruction of images of spatially varying dynamics.[13] We have investigated this possibility. We use an inversion algorithm, one of several possible schemes,[13,84] which is based on a solution to the correlation diffusion equation, Eq. (11), generalized to include spatially varying dynamics, $D_B(\mathbf{r}) = D_{B,o} + \delta D_B(\mathbf{r})$, absorption, $\mu_a(\mathbf{r}) = \mu_{a,o} + \delta\mu_a(\mathbf{r})$, and scattering, $\mu_s'(\mathbf{r}) = \mu_{s,o}' + \delta\mu_s'(\mathbf{r})$ and $D_\gamma(\mathbf{r}) = D_{\gamma,o} + \delta D_\gamma(\mathbf{r})$. $D_{B,o}$, $\mu_{s,o}'$, and $\mu_{a,o}$ are the spatially uniform background characteristics. $\delta\mu_a(\mathbf{r})$ is the spatial variation in the absorption coefficient, $\delta\mu_s'(\mathbf{r})$ is the spatial variation in the reduced scattering coefficient, $\delta D_\gamma(\mathbf{r})$ is the spatial variation in the photon-diffusion coefficient, and $\delta D_B(\mathbf{r})$ represents the spatial variation in the particle diffusion coefficient relative to the background value.

The steady-state correlation diffusion equation with spatially varying optical and dynamical properties is

$$\nabla^2 G_1(\mathbf{r}_s,\, \mathbf{r},\, \tau) - \frac{v\mu_{a,o}}{D_{\gamma,o}} G_1(\mathbf{r}_s,\, \mathbf{r},\, \tau)$$

$$- \frac{2v\mu_s'k_o^2 D_{B,o}\tau}{D_{\gamma,o}} G_1(\mathbf{r},\, \mathbf{r},\, \tau)$$

$$= -\frac{v}{D_\gamma(\mathbf{r})} S_o \delta(\mathbf{r}_s - \mathbf{r}) + \frac{1}{\mu_{s,o}'} \nabla\delta\mu_s'(\mathbf{r})$$

$$\cdot \nabla G_1(\mathbf{r}_s,\, \mathbf{r},\, \tau) + \frac{v\delta\mu_a(\mathbf{r})}{D_{\gamma,o}} G_1(\mathbf{r}_s,\, \mathbf{r},\, \tau)$$

$$+ \frac{2v\mu_s'k_o^2 \delta D_B(\mathbf{r})\tau}{D_{\gamma,o}} G_1(\mathbf{r}_s,\, \mathbf{r},\, \tau)$$

$$+ 3\mu_{a,o}\delta\mu_s' G_1(\mathbf{r}_s,\, \mathbf{r},\, \tau). \qquad (26)$$

This equation can be solved with the first Born approximation or the Rytov approximation.[84] Within the Rytov approximation we assume that $G_1(\mathbf{r}_s,\, \mathbf{r}_d,\, \tau) = G_1^o(\mathbf{r}_s,\, \mathbf{r}_d,\, \tau)\exp[\Phi_s(\mathbf{r}_s,\, \mathbf{r}_d,\, \tau)]$. Following the procedure described by Kak and Slaney,[84] we obtain an integral equation relating $\Phi_s(\mathbf{r}_s,\, \mathbf{r}_d,\, \tau)$ to the spatial variation of the dynamical and optical properties, i.e.,

$$\Phi_s(\mathbf{r}_s,\, \mathbf{r}_d,\, \tau) = -\frac{1}{G_1^o(\mathbf{r}_s,\, \mathbf{r}_d,\, \tau)}$$

$$\times \int \mathrm{d}^3 r' \left[\frac{2v\mu_s'k_o^2\tau\delta D_B(\mathbf{r}')}{D_{\gamma,o}} \right.$$

$$\times H(\mathbf{r}',\, \mathbf{r}_d,\, \tau) G_1^o(\mathbf{r}_s,\, \mathbf{r}',\, \tau)$$

$$+ \frac{v\,\delta\mu_a(\mathbf{r}')}{D_{\gamma,o}} H(\mathbf{r}',\, \mathbf{r}_d,\, \tau) G_1^o(\mathbf{r}_s,\, \mathbf{r}',\, \tau)$$

$$+ \left. \frac{\delta D_\gamma(\mathbf{r}')}{D_{\gamma,o}} \nabla G_1^o(\mathbf{r}_s,\, \mathbf{r}') \cdot \nabla H(\mathbf{r}',\, \mathbf{r}_d) \right].$$

$$(27)$$

Here $H(\mathbf{r}',\, \mathbf{r}_d,\, \tau)$ is the Green's function for the homogeneous correlation diffusion equation. The position of the source (detector) is $\mathbf{r}_s$ ($\mathbf{r}_d$).

There are many techniques that can be employed to invert Eq. (27).[13,84] All the methods are based on discretizing the integral equation and using measurements of $\Phi_s(\mathbf{r}_s,\, \mathbf{r}_d)$ with several different source–detector pairs to solve the coupled set of linear equations. We use the simultaneous iterative reconstruction technique[84] to solve the coupled equations.

To demonstrate that the correlation diffusion equation can be used as the basis for a tomographic reconstruction algorithm, we took several measurements of the correlation function on a solid, highly scattering sample that contained a spherical, dynamical region. The system was a solid cylinder of TiO_2 suspended in resin. The cylinder was homogeneous except for a 1.3-cm-diameter spherical cavity that was filled with an aqueous suspension of 0.296-μm polystyrene microspheres ($D_B = 1.5 \times 10^{-8}$ cm^2 s^{-1}) and centered at $z = 0$ (the z axis is the axis of the cylinder). The optical properties (μ_s', μ_a) of the colloid matched that of the solid so that we imaged only variations in the dynamical properties. Measurements were made every 30° at the surface of the cylinder for $z = 0,\ 1,\ 2$ cm, with source–detector angular separations of 30° and 170° and correlation times of $\tau = 15, 25, 35, 45, 55, 65, 75, 85$ μs. Except where the measurements were made, a highly reflective coating was applied to the surface so that the cylindrical medium could be better approximated as infinite. This approximation was discussed by Haskell et al.,[83] and its validity allows us to obtain accurate reconstructions of the dynamical properties.

The image of $D_B(\mathbf{r})$ shown in Fig. 10 was reconstructed from ~600 measurements of the scattered correlation function, $\Phi_s(\mathbf{r}_s,\, \mathbf{r}_d,\, \tau)$, with 400 iterations of the simultaneous iterative reconstruction technique.[84] The $z = 0$ slice of the image is shown in Fig. 10(a). From this image the center (in the x–y plane) of the dynamic region and the magnitude of the particle diffusion coefficient are determined. The center of the object in the image is within 2 mm of the actual center of the dynamic sphere. This discrepancy scales with the uncertainty in the position of the source and the detector. The sphere diameter (~1.3 cm) and the particle diffusion coefficient (~1.8 $\times 10^{-8}$ cm^2 s^{-1}) obtained from the imaging procedure also agree reasonably well with experimentally known parameters (1.3 cm and 1.5×10^{-8} cm^2 s^{-1}).

C. Validity of Diffusion Equation for Media with Spatially Varying Flow Properties

The experiments described thus far demonstrate the diffusion and the scattering of correlation in turbid samples in which the dynamics are governed by Brownian motion. The correlation diffusion equation can be modified to account for other dynamical processes. In the cases of random flow and shear flow the correlation diffusion equation becomes

$$(D_\gamma\nabla^2 - v\mu_a - 2v\mu_s'D_B k_o^2\tau - \tfrac{1}{3} v\mu_s'\langle\Delta V^2\rangle k_o^2\tau^2$$

$$- \tfrac{1}{15} v\mu_s'^{-1}\Gamma_{\mathrm{eff}}^2 k_o^2\tau^2)G_1(\mathbf{r},\, \tau) = -vS(\mathbf{r}). \qquad (28)$$

The fourth and the fifth terms on the left-hand side of Eq. (28) arise from random and shear flows, respectively. $\langle \Delta V^2 \rangle$ is the second moment of the particle speed distribution (assuming that the velocity distribution is isotropic and Gaussian),[30,85] and Γ_{eff} is the effective shear rate.[56] Notice that the dynamical absorption for flow in Eq. (28) increases as τ^2 (compared with the τ increase for Brownian motion) because particles in flow fields travel ballistically; also, D_B, $\langle \Delta V^2 \rangle$, and Γ_{eff} appear separately because the different dynamical processes are uncorrelated. The form of the dynamical absorption term for random flow is related to that for Brownian motion. Both are of the form $\frac{1}{3} v \mu_s' \langle \Delta r^2(\tau) \rangle$, where $\langle \Delta r^2(\tau) \rangle$ is the mean-square displacement of a scattering particle. For Brownian motion $\langle \Delta r^2(\tau) \rangle = 6 D_B \tau$, and for random flow $\langle \Delta r^2(\tau) \rangle = \langle \Delta V^2 \rangle \tau^2$. The derivation of the dynamical absorption term for shear flow is more complex, and the reader is referred to Wu et al.[56] for a complete discussion.

Flow in turbid media is an interesting problem that has received some attention. In these measurements experimenters typically determine a correlation function that may be a compound of many decays representing a weighted average of flow within the sample. For example, Bonner and Nossal developed an approach for
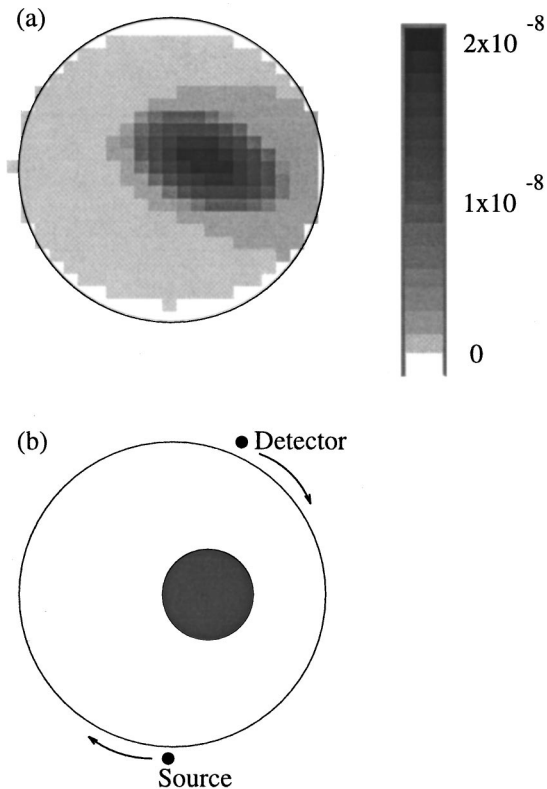

Fig. 10. (a) Image reconstructed from experimental measurements of the scattered correlation function. The system was a 4.6-cm-diameter cylinder with $l^* = 0.25$ cm, $\mu_a = 0.002$ cm^{-1}, and $D_B = 0$ [see illustration in (b)]. A 1.3-cm-diameter spherical cavity was centered at $x = 0.7$ cm, $y = 0$, and $z = 0$ and was filled with a colloid with $l^* = 0.25$ cm, $\mu_a = 0.002$ cm^{-1}, and $D_B = 1.5 \times 10^{-8}$ cm^2 s^{-1}. A slice of the image at $z = 0$ cm is presented in (a). The values of the reconstructed particle diffusion coefficients are indicated by the legend in units of square centimeters per second.

measuring random blood flow in homogeneous tissue[30]; Wu et al. applied DWS to study uniform shear flow[56]; and Bicout and co-workers applied DWS to study inhomogeneous flow and turbulence.[86–89] In all the cases, a priori knowledge of the flow is used in the analyses. The application of correlation diffusion imaging will further clarify information about heterogeneous flows in turbid media.

We conducted experiments to examine the correlation signal arising from a solid highly scattering medium with a single cylindrical vein containing a highly scattering liquid under Poiseuille flow. The experimental system is depicted in Fig. 11. In this experiment the correlation function is measured in remission from a semi-infinite, highly scattering, solid slab of TiO$_2$ suspended in resin ($\Gamma_{eff} = 0$). A 0.5% solution of Intralipid[90] is pumped through the cylindrical vein in the slab with pump speeds of 0.442 cm s^{-1}, 0.884 cm s^{-1}, and 1.77 cm s^{-1}. The experimental results are shown by the symbols in Fig. 12.

Measurements of the normalized temporal field correlation function were compared with the exact solution of correlation scattering from cylindrical inhomogeneities. The derivation of the analytic solution for a cylinder is similar to that for a sphere. Once again, the correlation is a superposition of the incident and the scattered correlation, i.e., $G_1^{out} = G_1^o + G_1^{scatt}$. For a cylinder of infinite length, the solution for the scattered wave in cylindrical coordinates is[66]

$$G_1^{scatt}(r, \theta, z)$$

$$= -\frac{vS}{2\pi^2 D_\gamma} \sum_{n=1}^{\infty} \int_0^{\infty} dp \; \cos(n\theta)\cos(pz)$$

$$\times \; K_n[\sqrt{p^2 - (K^{out})^2}r]K_n[\sqrt{p^2 - (K^{out})^2}r_s]$$

$$\times \left[\frac{D_\gamma^{out}x I_n'(x)I_n(y) - D_\gamma^{in}y I_n(x)I_n'(y)}{D_\gamma^{out}x K_n'(x)I_n(y) - D_\gamma^{in}y K_n(x)I_n'(y)} \right],$$

$$(29)$$

where I_n and K_n are modified Bessel functions, $x = \sqrt{p^2 - (K^{out})^2}a$, $y = \sqrt{p^2 - (K^{in})^2}a$, and a is the radius of the cylinder. We have simplified the solution by taking the z axis as the axis of the cylinder and assuming that the source is at $z = 0$ and $\theta = 0°$.

The comparison between experiment (symbols) and theory (curves) shown in Fig. 12 indicates a good agreement. The parameters used in the calculation, except for Γ_{eff}, were the known parameters. We determined the effective shear rate, Γ_{eff}, by fitting the analytic solution to the data with the constraint that Γ_{eff} had to scale linearly with the flow speed. The best fit to the data indicates that Γ_{eff} is approximately 6.8 cm^{-1} times the flow speed. Since the shear rate is given by the change in speed per unit length in the direction perpendicular to the flow, one might expect that the effective shear rate would be the flow speed divided by the radius of the vein. This simple calculation gives an effective shear rate that is a factor of 2 smaller than the measured Γ_{eff}. This difference is not yet understood, but it could result from the mismatches in optical indices of refraction and sensitivity to the semi-infinite boundary condition.
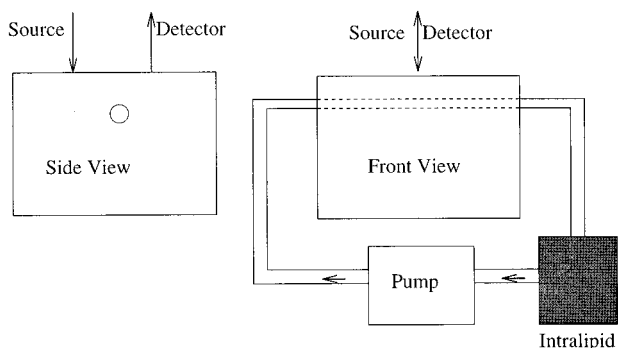
Fig. 11.   Same experimental system as that described in Fig. 6, except that the TiO_2 slab now has a 6-mm-diameter cylindrical cavity instead of a spherical cavity.   The cylindrical cavity is centered 13 mm below the surface of the slab, and 0.5% Intralipid is pumped through the cavity at flow speeds of 0.442, 0.884, and 1.77 cm s^{-1}.   For the solid slab, $\mu_s' = 4.0$ cm^{-1} and $\mu_a = 0.002$ cm^{-1}.   For the Intralipid, the optical properties are assumed to be the same as those of the TiO_2 slab.   The correlation function is measured with the source and the detector separated by 2.0 cm, i.e., the source is 1.0 cm to the left of the vein, and the detector is 1.0 cm to the right.
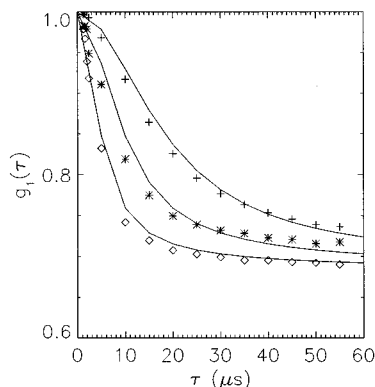
Fig. 12.   Experimental measurements of the normalized temporal field correlation function for three different flow speeds in comparison with theory.   Measurements for flow speeds of 0.442, 0.884, and 1.77 cm s^{-1} are indicated by the symbols +, *, and $\diamond$, respectively.   The curves, from top to bottom, are calculated with the experimental parameters given in Fig. 11 and with effective shear rates of 3.0, 6.0, and 12.0 s^{-1}, respectively.

D.   Burn Phantoms

The noninvasive determination of the depth of severe burns has been an intriguing problem for several years. A robust solution would offer medical practitioners a valuable tool for diagnosing and treating severe burns. Burned tissue is essentially a turbid medium with spatially varying dynamics; i.e., light is multiply scattered by the tissue, and layers of burned tissue are characterized by a lack of blood flow (blood flow ceases in severely burned tissue).   Here we show that diffusing correlation can be used to distinguish static layers that differ in thickness by 100 μm and that the correlation diffusion equation predicts the observed correlation function fairly well.   These positive results motivated animal studies, the results of which are presented in Section 6.

The burn phantom is drawn in Fig. 13(a).   It consists of a layer of Teflon resting on a solution of Intralipid.

The Teflon mimics tissue that has been severely burned in that the Teflon scatters light, and the scattering particles are static.   The Intralipid simulates the scattering and dynamical properties of the healthy tissue underlying the burned tissue.   For the Teflon, $\mu_s' = 79$ cm^{-1} and μ_a is negligibly small.   We used a 3.75% solution of Intralipid, for which $\mu_s' = 55$ cm^{-1} and μ_a is negligibly small.   For both the Teflon and the Intralipid solution the absorption was taken to be 0.002 cm^{-1}.   The effective Brownian diffusion coefficient of the globules in the Intralipid solution is approximately 10^{-8} cm^2 s^{-1}, as determined from the mean diameter of 0.4 μm for the globules. Thicknesses of Teflon ranging from 0.132 to 0.802 mm are used in the experiments to mimic burns of different depths.

Figure 13(b) plots the normalized field temporal correlation function for different Teflon thicknesses with a source–detector separation of 1.2 mm.   A significant difference is observed in the rates of decay for different Teflon thicknesses.   Figure 13(b) indicates that these correlation measurements are sensitive to changes in the Teflon thickness smaller than 100 μm.

These measurements can be modeled with a solution of the correlation diffusion equation for the system depicted in Fig. 13(a).   To solve the diffusion equation, we approximate the collimated source as an isotropic point source displaced a distance $z_o = 1/\mu_s'$ into the medium along the axis of the collimated source.   We also use the approxi-
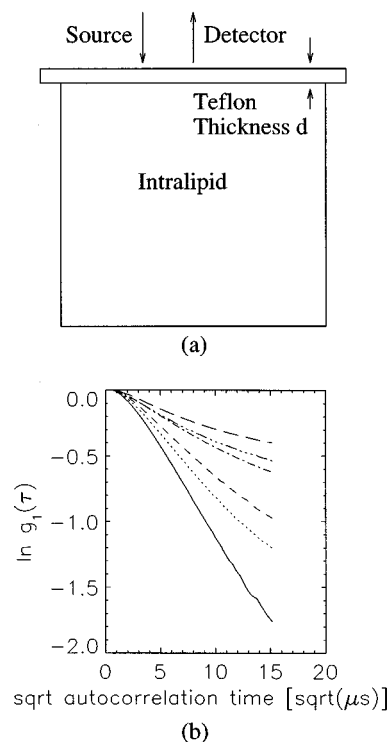

(a)

(b)

Fig. 13.   (a) Schematic of the burn phantom.   In (b) the natural log of the normalized field correlation function is plotted versus the square root (sqrt) of the correlation time for different Teflon thicknesses.   The source–detector separation was held fixed at 1.2 mm.   The solid curve is for a thickness of 0.132 mm.   The other curves, in order of decreasing slope, are for thicknesses of 0.258, 0.408, 0.517, 0.650, and 0.802 mm.

mate extrapolated-zero boundary condition instead of the exact zero-flux boundary condition (partial flux in the case of an index mismatch). For the extrapolated-zero boundary condition the field correlation is taken to be zero at $z = z_b = -2/(3\mu_s')$, where the physical boundary is at $z = 0$. The diffusion equation must be solved for two cases: (1) when the point source is in the static layer, and (2) when the point source is displaced into the dynamic region [see Fig. 13(a)]. In the first case, $G_1(\mathbf{r}, \tau)$ measured on the surface of the static layer a distance ρ from the source is given by

$$
\begin{aligned}
G_1(\mathbf{r},\ \tau) \\
= \frac{\exp[-k_1(\tau)\sqrt{\rho^2 + z_o{}^2}]}{4\pi\sqrt{\rho^2 + z_o{}^2}} \\
- \frac{\exp[-k_1(\tau)\sqrt{\rho^2 + (z_o + 2z_b)^2}]}{4\pi\sqrt{\rho^2 + (z_o + 2z_b)^2}} \\
+ \int_0^\infty \lambda\,\mathrm{d}\lambda A(\lambda)J_0(\lambda\rho)\frac{\sin[\sqrt{k_1{}^2(\tau) - \lambda^2}(z + z_b)]}{\sqrt{k_1{}^2(\tau) - \lambda^2}}.
\end{aligned}
$$

$$(30)$$

Here $k_1{}^2(\tau) = v^{(1)}\mu_a^{(1)}/D_\gamma^{(1)}$ is the correlation wave number in the static layer, $J_0(x)$ is a cylindrical Bessel function, and $A(\lambda)$ is a constant that depends on the thickness of the static layer and on the properties of the dynamical medium. This constant is

$$
\begin{aligned}
A(\lambda) = -\{\exp[iX(\lambda)(d - z_o)] - \exp[iX(\lambda)(d + 2z_b + z_o)]\} \\
\times \frac{D_\gamma^{(2)}Y(\lambda) - D_\gamma^{(1)}X(\lambda)}{D_\gamma^{(1)}X(\lambda)\cos[X(\lambda)(d + z_b)] - iD_\gamma^{(2)}Y(\lambda)\sin[X(\lambda)(d + z_b)]},
\end{aligned}
$$

$$(31)$$

with $X(\lambda) = \sqrt{k_1{}^2(\tau) - \lambda^2}$ and $Y(\lambda) = \sqrt{k_2{}^2(\tau) - \lambda^2}$, where $k_2(\tau) = [v^{(2)}\mu_a^{(2)} + 2v\mu_s'^{(2)}D_Bk_o{}^2\tau]/D_\gamma^{(2)}$ is the correlation wave number in the dynamical medium.

The solution for the second case is

$$
G_1(\mathbf{r},\ \tau) = \int_0^\infty \lambda\,\mathrm{d}\lambda J_0(\lambda\rho)\frac{-2iD_\gamma^{(2)}\exp[iY(\lambda)(z_o - d)]}{D_\gamma^{(1)}X(\lambda)\cos[X(\lambda)(d + z_b)] - iD_\gamma^{(2)}Y\sin[X(\lambda)(d + z_b)]}\sin[X(\lambda)z_b]. \quad (32)
$$

Comparisons between experiment and diffusion theory are made in Fig. 14. The parameters used in the calculation are given in the text's discussion of Fig. 13(a). The agreement between experiment and theory, although not perfect, is pretty good and certainly captures the trend as a function of source–detector separation and static-layer thickness. It is interesting that the agreement is better at larger thicknesses, where the diffusion theory is expected to be more valid in the static layer. The larger disagreement at smaller thicknesses is most likely a result of the breakdown of the diffusion approximation in

the small static layer. In this regime comparison with a solution of the correlation transport equation[61,62] would be more appropriate.

5.   MONTE CARLO SIMULATIONS

This section presents the results of various Monte Carlo simulations of correlation diffusion. We used the results from Monte Carlo simulations to check the accuracy of the correlation diffusion equation when the accuracy of our experimental results was questionable or when we did not have the experimental data. These simulations allow us to obtain data for systems with no variation in the index of refraction. In many cases these simulations provide a signal-to-noise ratio that is difficult to achieve in the laboratory and therefore permit a more accurate test of the validity of the correlation diffusion theory.

We first present simulation results for an infinite, homogeneous system compared with correlation diffusion theory. This comparison illustrates the behavior of the correlation function as different parameters are varied. Good agreement with diffusion theory is observed. We then present results for a system that is infinite, static, and homogeneous, except for a spherical dynamic region. This system avoids the shortcomings of the experimental system used in Section 4. Results are compiled for a wide range of parameters and are compared with correlation diffusion theory. The agreement is good, indicating the robustness of the theory. We then present simulations for a two-component system with spatially uniform random flow in a spatially uniform static medium. This system models a capillary network in tissue. The comparison with correlation diffusion theory demonstrates that the homogeneous solution can be used as long as the dynamical term is weighted by

$$
\frac{\mu_s'(\text{random flow component})}{\mu_s'(\text{random flow component}) + \mu_s'(\text{static component})}.
$$

$$(33)$$

The Monte Carlo simulations for obtaining electric-field temporal autocorrelation functions are described in Subsection 3.B. Briefly, the approach is to histogram the accumulated momentum transfer of photons scattered from moving particles as they propagate through a system with spatially varying dynamics. That is, scattering events in a static medium do not contribute to the accumulated mo-
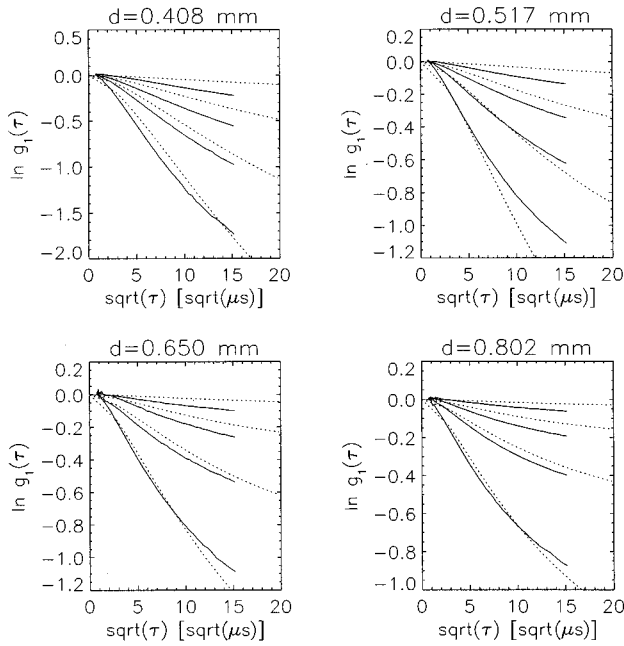
Fig. 14. Comparisons between the experimental data and those predicted by theory for different thicknesses and separations. Each graph shows the results for a particular thickness of Teflon. The solid curves are the experimental data, and the dotted curves are theoretical data. Results for separations of 0.4, 0.8, 1.2, and 1.8 mm are given.

mentum transfer, whereas scattering events in a dynamic medium do contribute. The contribution is proportional to the magnitude of the dynamics. In the simulation the momentum transfer is accumulated as a dimensionless variable that scales with $k_o{}^2$. The histogram, when normalized, is the momentum-transfer probability distribution $P(Y)$. The correlation function can then be calculated with[74,75]

$$g_1(\tau) = \int_0^\infty dY P(Y) \exp\left[-\frac{1}{3} Y k_o{}^2 \langle \Delta r^2(\tau) \rangle\right]. \quad (34)$$

$P(Y)$ is determined from the Monte Carlo simulation, $k_o{}^2$ is the wave number of light in the medium, and $\langle \Delta r^2(\tau) \rangle$ is determined by the dynamics of the system.

A. Homogeneous Media with Brownian Motion
Figure 15 plots the Monte Carlo results and the predictions of theory [Eq. (13)] for different source–detector separations ρ in an infinite medium. The optical and the dynamical properties are held constant at $\mu_s{}' = 10.0$ cm^{-1}, $\mu_a = 0.05$ cm^{-1}, and $D_B = 1 \times 10^{-8}$ cm^2 s^{-1}. The decay rate of $g_1(\tau)$ increases linearly with ρ, as expected. Next, we can see the plateau at early τ and that the transition time is independent of ρ. Finally, $g_1(\tau)$ calculated with correlation diffusion theory for the different source–detector separations is given by the curves. In all the cases good agreement is observed when $k_o{}^2 \langle \Delta r^2(\tau) \rangle \ll 1$. As expected, the agreement is not good at longer correlation times because of the breakdown of the approximation that $k_o{}^2 \langle \Delta r^2(\tau) \rangle \ll 1$. The results indicate that the approximation is not valid when $k_o{}^2 \langle \Delta r^2(\tau) \rangle \gtrsim 0.1$, that is, when $\tau \gtrsim 225$ μs.

The behavior of the deviation is understood. At longer correlation times the decay results from shorter photon path lengths, since the longer path lengths have a faster decay rate and no longer provide a significant contribution. For the shorter path lengths the photon-diffusion approximation is not valid, inasmuch as the photons are not diffusing. Furthermore, the q average is not appropriate, since there have been only a few scattering events, and, for the photon to reach the detector, the scattering angles must be smaller than average. The smaller-than-average scattering angles result in the observed slower decay rate of the Monte Carlo simulations relative to diffusion theory.

B. Media with Spatially Varying Brownian Motion
Here we present Monte Carlo results to check the validity of the correlation diffusion equation for systems with spatially varying dynamical and optical properties. The system is infinite, static, and homogeneous, except for a spherical region that is dynamic and may have different optical properties than the background. The homogeneous properties are $\mu_s{}' = 10.0$ cm^{-1} and $D_B = 0$. For the sphere, $\mu_s{}' = 10.0$ cm^{-1} and $D_B = 1 \times 10^{-8}$ cm^2 s^{-1}. The absorption coefficients are varied. Results are presented for the source–detector positions indicated in Fig. 16(a).

Comparison of Monte Carlo results and correlation diffusion theory for a system with spatially varying dynamical properties but uniform optical properties is presented in Figs. 16(b)–16(d). Three different absorption coefficients are considered. In Figs. 16(b), 16(c), and 16(d) the absorption coefficients are $\mu_a = 0.02$ cm^{-1}, μ_a
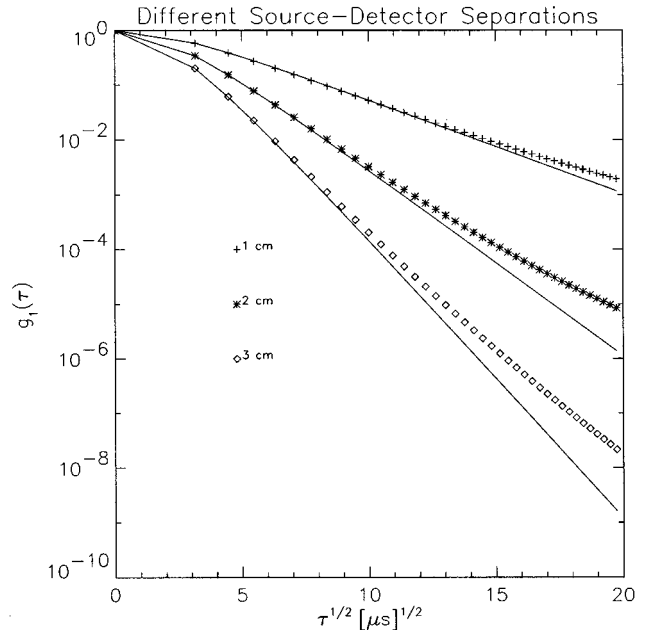

Fig. 15. Comparison between Monte Carlo simulations for correlation diffusion in a homogeneous medium and predictions of theory for different source–detector separations. Monte Carlo results are given by the symbols. The solid curves are calculated from diffusion theory. $\mu_s{}' = 10.0$ cm^{-1}, $\mu_a{}' = 0.05$ cm^{-1}, and $D_B = 1.0 \times 10^{-8}$ cm^2 s^{-1}.
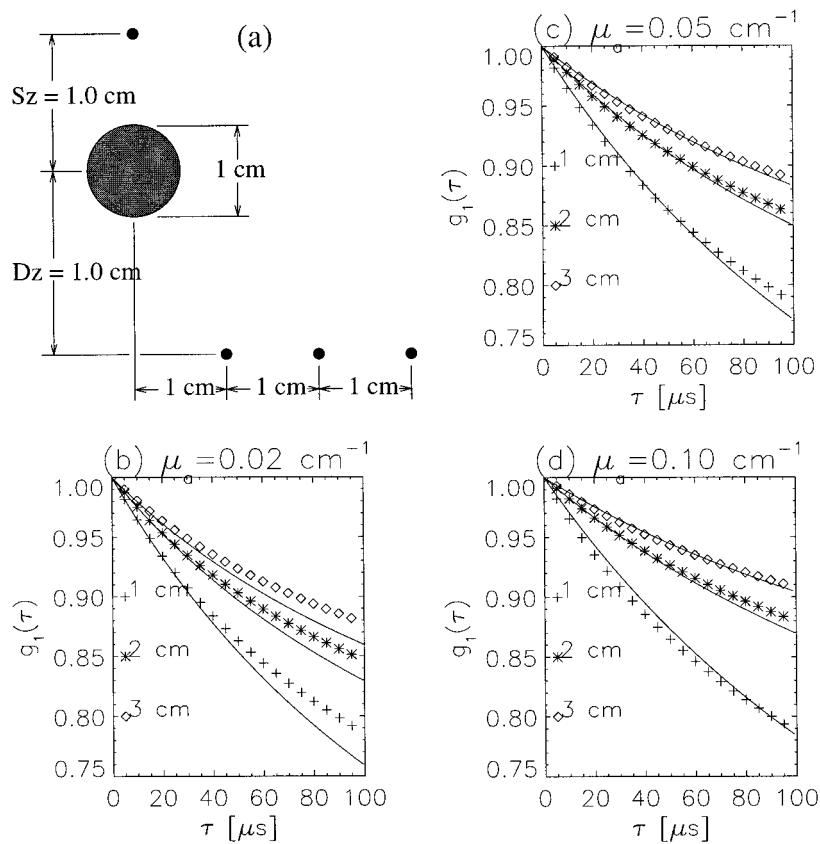
Fig. 16.   Comparison between Monte Carlo results for the $g_1(\tau)$ (symbols) and correlation diffusion theory (solid curves) for the system depicted in (a).   An isotropic point source is positioned 1.0 cm from the center of a spherical inhomogeneity.   The sphere has a diameter of 1 cm.   Detectors are positioned 1.0 cm away along the z axis and are displaced off the z axis at $\rho = 1, 2, 3$ cm.   The optical properties are spatially uniform.   In (b), (c), and (d) the absorption coefficient $\mu_a = 0.02, 0.05, 0.10$ cm^{-1}, respectively.   The ρ position of the detector is indicated in the legend.

$= 0.05$ cm^{-1}, and $\mu_a = 0.10$ cm^{-1}, respectively.   For each absorption coefficient, results are presented for the three detector positions.   The Monte Carlo results are given by the symbols, and the curves indicate the prediction of correlation diffusion theory.   The agreement is fairly good.   For other Brownian diffusion coefficients, τ scales inversely with D_B, as expected and as observed experimentally (see Fig. 9).

The small discrepancies are most likely due to the fact that a significant fraction of the fluctuating photons have scattered from the dynamical region only a few times before detection.[39]   By "fluctuating photons" we mean those photons that have sampled the dynamic region as opposed to the static photons that have not seen the dynamic region.

C.   Media with Random Flow

Tissue blood flow is a good example of an optically turbid medium with random flow.   Capillary networks are generally randomly oriented on length scales set by the photon random-walk step length.   When the capillary flow is oriented, as it is in muscle, the photon generally scatters 10+ times between interactions with blood such that the photon's direction is randomized between blood interactions.   Thus the flow is effectively random.   Tissue blood flow can be modeled as a two-component system, the
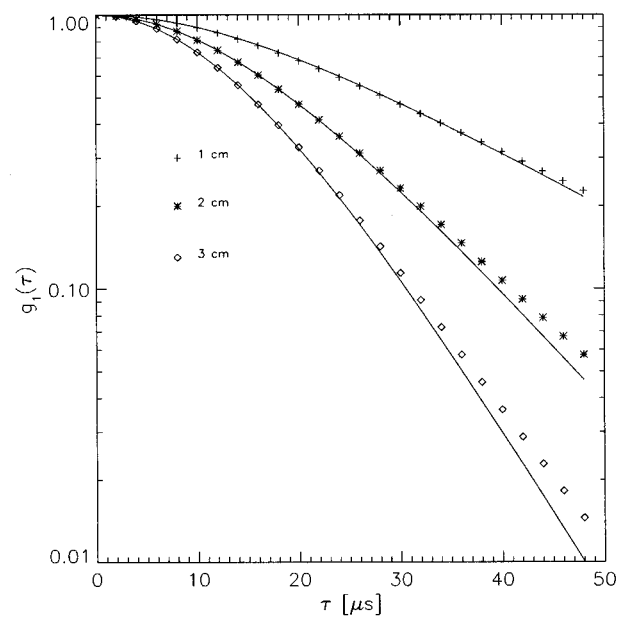

Fig. 17.   Comparison of Monte Carlo simulations and correlation diffusion theory for random flow in a static tissuelike matrix. The probability of scattering from a flow particle (blood) is 0.1.

static tissue matrix and the randomly flowing blood.[30,91] Monte Carlo results for this system are compared with correlation diffusion theory predictions.

Because the system is composed of two uniformly distributed components, it is necessary to modify the correlation diffusion equation to account for the volume fraction of blood. One does this by simply weighting the dynamical absorption term by the probability of scattering from a red blood cell, i.e.,

$$(D_\gamma \nabla^2 - v\mu_a - \tfrac{1}{3}P_{\text{blood}}v\mu_s'k_o^2\langle\Delta V^2\rangle\tau^2)G_1(\mathbf{r},\ \tau)$$
$$= -vS(\mathbf{r}).\quad (35)$$

P_{blood} is the probability of scattering from a red blood cell and is given by

$$P_{\text{blood}} = \frac{\mu_s'(\text{blood})}{\mu_s'(\text{blood}) + \mu_s'(\text{static component})}.\quad (36)$$

The other optical parameters in Eq. (35) account for the combined contribution from the tissue matrix and the blood.

A comparison of the Monte Carlo results and correlation diffusion theory is presented in Fig. 17 for P_{blood} = 0.1   The optical properties are μ_s' = 10.0 cm^{-1} and μ_a = 0.05 cm^{-1}. The mean-square speed of the red blood cells is $\langle\Delta V^2\rangle$ = 1.0 mm^2 s^{-2}. The agreement is quite good when $k_o^2\langle\Delta V^2\rangle\tau^2 \ll 1$, indicating that the diffusion theory can be used to quantify blood flow in particular and random flow in turbid media in general. The small discrepancy observed for times greater than 25 μs arises from the assumption that $k_o^2\langle\Delta V^2\rangle\tau^2 \ll 1$ [note that $(k_o^2\langle\Delta V^2\rangle)^{-1/2}$ = 61 μs]. Comparisons were made for other P_{blood} values, and in all the cases good agreement was observed.

6. DIAGNOSING TISSUE BURN DEPTH

After verifying with measurements on phantoms that photon correlation techniques are sensitive to differences in thickness of 100 μm and that the correlation diffusion equation [Eq. (11)] can be used to model the correlation function (see Subsection 4.D), we applied diffuse correlation spectroscopy in a clinical environment. The clinical work was done with Norm Nishioka and Kevin Schomacker at the Wellman Institute in Boston, Massachusetts. We used their pig burn model and protocol for the clinical trials.[92]

To probe burn depth, we used the experimental system depicted in Fig. 18. The laser light is coupled into a multimode optical fiber (core diameter, 200 μm). This fiber delivers the light to the pig. Several single-mode fibers are positioned with the source fiber to collect light at distances ranging from 0.2 to 2.4 mm from the source. The light collected with the single-mode fibers is then delivered to a photon-counting PMT and is analyzed with a digital temporal autocorrelator. In the experiments presented here, approximately 4 mW of light is incident upon the sample, and the signal is integrated for 1 min. The pig was anesthetized and was stabilized on an operating table in an operating suite at the Wellman Institute. Burns were administered with 2-in.-square metal blocks brought to 100 °C by means of boiling water. Burn thick-

ness was controlled by application of the metal block to the skin for a duration of 1–20 s. For our study, five different burns were examined. The duration and the depth of each burn is provided in Table 1. The measurements were made 48 h after administration of the burn.

Prior to burning the tissue, measurements were made at various positions on the skin to determine a baseline. Also, baselines were periodically measured on healthy tissue between measurements of the burned tissue. For the healthy tissue, we observed a single exponential decay in the correlation function and saw that the decay rate increased linearly with the source–detector separation.

Figure 19 plots the temporal field correlation functions obtained from the 48-h-old burns for a source–detector separation of 800 μm. As expected, the decay rate of the correlation function decreases as the burn thickness increases. These data indicate that the 5-, 7-, 12-, and 20-s, burns are easily distinguished. To summarize the data for all the source–detector separations, we determined the decay rate of the correlation function for $0 < \tau < 100$ μs by fitting a line to the data, and we plot the decay rate as a function of source–detector separation for different burns. These results are given in Fig. 20
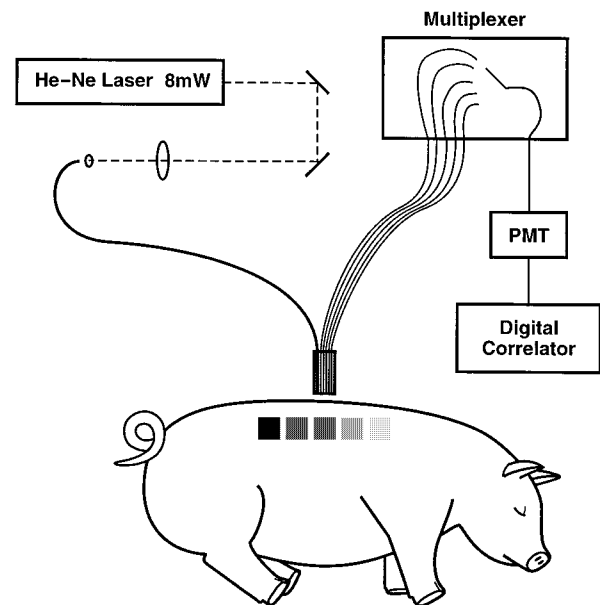

Fig. 18.   Experimental setup for the pig experiments.   The shaded areas on the pig indicate burns of various depths.

Table 1. Burn Depths Were Assessed from Biopsied Tissue by Use of a Lactate Dehydrogenase Stain[a]

Duration of Burn (s)	Burn Depth (μm)
3	60–100 (epidermal)
5	400–500
7	500–600
12	1500–2000
20	2100–2200

[a] Lactate dehydrogenase is a vital stain; therefore it will not stain cells that are deadened by the burn.
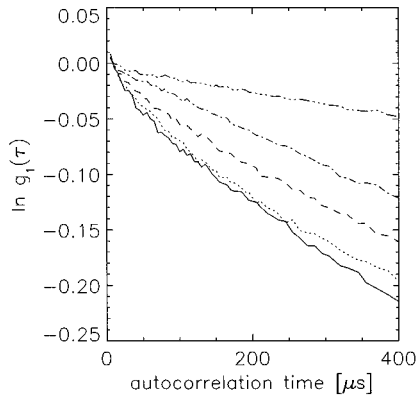
Fig. 19. Plot of temporal field correlation functions obtained from the 48-h-old burns for a source–detector separation of 800 μm. The correlation functions for the 3-s (solid curve), 5-s (dotted curve), 7-s (dashed curve), 12-s (dotted–dashed curve), and the 20-s (top curve) burns are presented.
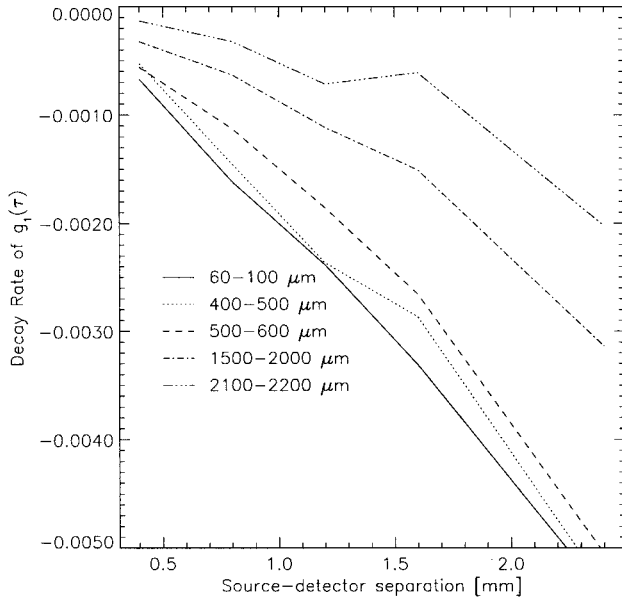

Fig. 20. Graph of decay rate of the correlation function versus source–detector separation for different burns. The burn depths are indicated in the legend.

and indicate that it is possible to distinguish burns that vary in thickness by only 100 μm. The behavior of the decay rate is expected. For shallow burns, the decay rate increases linearly with the source–detector separation, as observed for healthy tissue and as expected for a homogeneous system; i.e., the shallow burn does not perturb the correlation function. However, for deeper burns, the decay rate decreases and no longer increases linearly with the source–detector separation.

Our results from this clinical study are encouraging in that they verify that correlation measurements can be used to distinguish burns with thicknesses that vary by 100 μm. More research is needed to quantify the burn thickness from the raw data. The quantification will require knowledge of the optical and the dynamical properties of the burn. It should be possible to determine these

quantities from the correlation measurements and from diffuse reflectance measurements in the time domain and/or the frequency domain. One may simplify this quantification by comparing correlation functions between burned and healthy tissue. A ratio of such measurements may be insensitive to blood flow, thus reducing the number of unknowns in the determination of the burn depth. Finally, the behavior of the burns during the first few hours must be studied carefully to determine whether correlation techniques can be used to diagnose the severity of fresh burns. To be a suitable diagnostic tool, our technique must be able to characterize burns during the first day, preferably within the first 6 h. This research is in progress.

7. SUMMARY

We have shown that the transport of temporal electric-field correlation through turbid media can be modeled with a diffusion equation and is thus completely analogous to photon diffusion. The properties of diffusing correlation are thus expected to be similar to the properties of photon diffusion. We demonstrated this experimentally by showing that the migration of correlation in a turbid medium with spatially varying dynamical and optical properties can be viewed as a macroscopic scattering of correlation waves. This concept was shown in the context of both forward and inverse problems. The inverse problem, otherwise known as image reconstruction methods, offers exciting possibilities for studying dynamical variations in heterogeneous turbid media. In biomedical optics, for example, this approach offers a simple framework for analyzing the complex signals obtained from fluid flow in the body.

APPENDIX A: DIFFUSION APPROXIMATION TO THE CORRELATION TRANSPORT EQUATION

The P_N approximation as described for the photon transport equation[93–96] can be applied to the correlation transport equation with only a few modifications. The correlation transport equation is

$$\nabla \cdot G_1{}^T(\mathbf{r}, \hat{\Omega}, \tau)\hat{\Omega} + \mu_t G_1{}^T(\mathbf{r}, \hat{\Omega}, \tau)$$

$$= \mu_s \int G_1{}^T(\mathbf{r}, \hat{\Omega}', \tau)g_1{}^s(\hat{\Omega}, \hat{\Omega}', \tau)f(\hat{\Omega}, \hat{\Omega}')d\hat{\Omega}'$$

$$+ S(\mathbf{r}, \hat{\Omega}). \tag{A1}$$

Here $G_1{}^T(\mathbf{r}, \hat{\Omega}, \tau)$ is the unnormalized temporal field correlation function, which is a function of position $\mathbf{r}$, direction $\hat{\Omega}$, and correlation time τ. The scattering and the absorption coefficients are μ_s and μ_a, respectively, and $\mu_t = \mu_s + \mu_a$ is the transport coefficient. Furthermore, $g_1{}^s(\hat{\Omega}, \hat{\Omega}', \tau)$ is the normalized temporal field correlation function for single scattering; $f(\hat{\Omega}, \hat{\Omega}')$ is the normalized differential cross section; and $S(\mathbf{r}, \hat{\Omega})$ is the source distribution. The scattering coefficient is the reciprocal of the scattering length, $\mu_s = 1/l$, and the absorption coefficient is the reciprocal of the absorption length, $\mu_a = 1/l_a$. The time dependence (not to be confused with correlation

time) has been left out of the equation since we are considering only measurements with cw sources. We can include the time dependence by adding a time derivative of $G_1^T(\mathbf{r}, \hat{\Omega}, \tau)$ {i.e., $v^{-1}[\partial/(\partial t)]G_1^T(\mathbf{r}, \hat{\Omega}, \tau)$} to the left-hand side of Eq. (A1).

In analogy to photon transport, the correlation fluence is

$$G_1(\mathbf{r}, t) = \int d\hat{\Omega} G_1^T(\mathbf{r}, \hat{\Omega}, \tau), \qquad (A2)$$

whereas the correlation flux is given by

$$\mathbf{J}_g(\mathbf{r}, t) = \int d\hat{\Omega} G_1^T(\mathbf{r}, \hat{\Omega}, \tau)\hat{\Omega}. \qquad (A3)$$

The main difference between the correlation transport equation and the photon transport equation is the appearance of $g_1^s(\hat{\Omega}, \hat{\Omega}', \tau)$ in the integral. The appearance of this angular dependent quantity will result in integrals of three spherical harmonics, which are handled in a fashion similar to the handling of $\hat{\Omega} \cdot \nabla \phi_{l,m}(\mathbf{r}, t)$ in the photon transport equation.[93–96]

Within the P_N approximation, $G_1^T(\mathbf{r}, \hat{\Omega}, \tau)$ and the source distribution are expanded as

$$G_1^T(\mathbf{r}, \hat{\Omega}, \tau) = \sum_{l=0}^{N} \sum_{m=-l}^{l} \Gamma_{l,m}(\mathbf{r}, \tau)Y_{l,m}(\hat{\Omega}), \qquad (A4)$$

$$S(\mathbf{r}, \hat{\Omega}) = \sum_{l=0}^{N} \sum_{m=-l}^{l} q_{l,m}(\mathbf{r})Y_{l,m}(\hat{\Omega}). \qquad (A5)$$

For the phase function, we make the reasonable assumption that the amplitude is dependent only on the change in direction of the photon, and thus

$$f(\hat{\Omega} \cdot \hat{\Omega}') = \sum_{l=0}^{\infty} \frac{2l+1}{4\pi} g_l P_l(\hat{\Omega} \cdot \hat{\Omega}')$$

$$= \sum_{l=0}^{\infty} \sum_{m=-l}^{l} g_l Y_{l,m}^*(\hat{\Omega}')Y_{l,m}(\hat{\Omega}), \qquad (A6)$$

where P_l is a Legendre polynomial and the second line is obtained with the angular addition rule.[97] The phase function is normalized, and therefore $g_0 = 1$.

The single-scattering temporal field correlation function is

$$g_1^s(\hat{\Omega}, \hat{\Omega}', \tau) = \exp[-\tfrac{1}{6}q^2\langle \Delta r^2(\tau)\rangle]$$

$$= \exp[-\tfrac{1}{3}k_o^2\langle \Delta r^2(\tau)\rangle(1 - \hat{\Omega} \cdot \hat{\Omega}')], \qquad (A7)$$

where $\langle \Delta r^2(\tau)\rangle$ is the mean-square displacement of the scattering particles and $q = 2k_o \sin(\theta/2)$ is the momentum transfer for the scattered photon, where θ is the angle between $\hat{\Omega}$ and $\hat{\Omega}'$. For particles undergoing Brownian motion, $\langle \Delta r^2(\tau)\rangle = 6D_B\tau$, where D_B is the Brownian diffusion coefficient. When $\tau \ll (2D_B k_o^2)^{-1}$, then Eq. (A7) is Taylor expanded to

$$g_1^s(\hat{\Omega}, \hat{\Omega}', \tau) = 1 - 2D_B k_o^2\tau + 2D_B k_o^2\tau(\hat{\Omega} \cdot \hat{\Omega}')$$

$$= 1 - 2D_B k_o^2\tau + 2D_B k_o^2\tau \frac{4\pi}{3}$$

$$\times \sum_{m=-1}^{1} Y_{1,m}^*(\hat{\Omega}')Y_{1,m}(\hat{\Omega}). \qquad (A8)$$

The second line is obtained with the angular addition rule.[97] Note that $(2D_B k_o^2)^{-1} \approx 10^{-3}$ s when $D_B = 1 \times 10^{-8}$ cm^2 s^{-1} and the wavelength of light is 514 nm.

Substituting these expansions into the correlation transport equation, Eq. (A1), we obtain

$$\sum_{l=0}^{N} \sum_{m=-l}^{l} \left\{ (\hat{\Omega} \cdot \nabla + \mu_t)\Gamma_{l,m}(\mathbf{r}, \tau)Y_{l,m}(\hat{\Omega}) \right.$$

$$- q_{l,m}Y_{l,m}(\hat{\Omega}) - \mu_s \int d\hat{\Omega}' \Gamma_{l,m}(\mathbf{r}, \tau)Y_{l,m}(\hat{\Omega}')$$

$$\times \sum_{l'=0}^{N} \sum_{m'=-l}^{l} g_{l'} Y_{l',m'}^*(\hat{\Omega}')Y_{l',m'}(\hat{\Omega})\left[1 - 2D_B k_o^2\tau \right.$$

$$\left. \left. + 2D_B k_o^2\tau \frac{4\pi}{3} \sum_{m''=-1}^{1} Y_{1,m''}^*(\hat{\Omega}')Y_{1,m''}(\hat{\Omega}) \right] \right\} = 0.$$
$$(A9)$$

The integral over $\hat{\Omega}'$ can be calculated for the first two terms between the brackets on the third and fourth lines by use of the spherical harmonic orthogonality relation. Integrating gives

$$\sum_{l=0}^{N} \sum_{m=-l}^{l} [\hat{\Omega} \cdot \nabla + \mu_t^{(l)} + g_l k_c]\Gamma_{l,m}(\mathbf{r}, \tau)Y_{l,m}(\hat{\Omega})$$

$$- q_{l,m}Y_{l,m}(\hat{\Omega}) - k_c \int d\hat{\Omega}' \Gamma_{l,m}(\mathbf{r}, \tau)Y_{l,m}(\hat{\Omega}')$$

$$\times \sum_{l'=0}^{N} \sum_{m'=-l}^{l} g_{l'} Y_{l',m'}^*(\hat{\Omega}')Y_{l',m'}(\hat{\Omega})$$

$$\times \left[\frac{4\pi}{3} \sum_{m''=-1}^{1} Y_{1,m''}^*(\hat{\Omega}')Y_{1,m''}(\hat{\Omega}) \right] = 0. \quad (A10)$$

New notation is introduced to simplify Eq. (A10): $\mu_t^{(l)} = \mu_s(1 - g_l) + \mu_a$ is the reduced transport coefficient [note that $\mu_t^{(0)} = \mu_a$], and $k_c = 2\mu_s D_B k_o^2\tau$ is a dynamic absorption coefficient.

$Y_{1,m''}^*(\hat{\Omega}')Y_{l',m'}^*(\hat{\Omega}')$ and $Y_{1,m''}(\hat{\Omega})Y_{l',m'}(\hat{\Omega})$ can be rewritten in terms of single spherical harmonics, given (see Arfken,[98] Section 12.9) as

$$Y_{l,m}(\hat{\Omega})Y_{1,-1}(\hat{\Omega}) = \sqrt{\frac{3}{8\pi}} B_{l+1}^{m-1}Y_{l+1,m-1}(\hat{\Omega})$$

$$- \sqrt{\frac{3}{8\pi}} B_l^{-m}Y_{l-1,m-1}(\hat{\Omega}), \qquad (A11)$$

$$Y_{l,m}(\hat{\Omega})Y_{1,0}(\hat{\Omega}) = \sqrt{\frac{3}{4\pi}} A_{l+1}^m Y_{l+1,m}(\hat{\Omega})$$

$$+ \sqrt{\frac{3}{4\pi}} A_l^m Y_{l-1,m}(\hat{\Omega}), \qquad (A12)$$

$$Y_{l,m}(\hat{\Omega})Y_{1,1}(\hat{\Omega}) = \sqrt{\frac{3}{8\pi}}\, B_{l+1}{}^{-m-1}Y_{l+1,m+1}(\hat{\Omega})$$

$$- \sqrt{\frac{3}{8\pi}}\, B_l{}^m Y_{l-1,m+1}(\hat{\Omega}). \qquad (A13)$$

The product of spherical harmonics in the integral of Eq. (A10) can be rewritten as

$$\frac{4\pi}{3}\sum_{l'm'} g_{l'}Y_{l'}{}^{m'*}(\hat{\Omega}')Y_{l'}{}^{m'}(\hat{\Omega})\sum_{m''=-1}^{1} Y_1{}^{m''*}(\hat{\Omega}')Y_1{}^{m''}(\hat{\Omega})$$

$$= \frac{4\pi}{3}\sum_{l'm'} g_{l'}\left\{\frac{3}{8\pi}\left[B_{l'+1}{}^{m'-1}Y_{l'+1}{}^{m'-1*}(\hat{\Omega}')\right.\right.$$

$$\left.- B_{l'}{}^{-m'}Y_{l'-1}{}^{m'-1*}(\hat{\Omega}')\right][B_{l'+1}{}^{m'-1}Y_{l'+1}{}^{m'-1}(\hat{\Omega})$$

$$- B_{l'}{}^{-m'}Y_{l'-1}{}^{m'-1}(\hat{\Omega})]$$

$$+ \frac{3}{4\pi}[A_{l'+1}{}^{m'}Y_{l'+1}{}^{m'*}(\hat{\Omega}')$$

$$+ A_{l'}{}^{m'}Y_{l'-1}{}^{m'*}(\hat{\Omega}')][A_{l'+1}{}^{m'}Y_{l'+1}{}^{m'}(\hat{\Omega})$$

$$+ A_{l'}{}^{m'}Y_{l'-1}{}^{m'}(\hat{\Omega})] - \frac{3}{8\pi}$$

$$\times [B_{l'+1}{}^{-m'-1}Y_{l'+1}{}^{m'+1*}(\hat{\Omega}')$$

$$- B_{l'}{}^{m'}Y_{l'-1}{}^{m'+1*}(\hat{\Omega}')][B_{l'+1}{}^{-m'-1}Y_{l'+1}{}^{m'+1}(\hat{\Omega})$$

$$\left.- B_{l'}{}^{m'}Y_{l'-1}{}^{m'+1}(\hat{\Omega})]\right\}. \qquad (A14)$$

Performing the final integral over $\hat{\Omega}'$, we obtain

$$\sum_{l=0}^{N}\sum_{m=-l}^{l}[\hat{\Omega}\cdot\nabla + \mu_t^{(l)} + g_l k_c]\Gamma_{l,m}(\mathbf{r},\tau)Y_{l,m}(\hat{\Omega})$$

$$- q_{l,m}Y_{l,m}(\hat{\Omega}) - k_c\Gamma_{l,m}\frac{4\pi}{3}$$

$$\times\left\{\frac{3}{8\pi}g_{l-1}B_l{}^m[B_l{}^m Y_l{}^m(\hat{\Omega}) - B_{l-1}{}^{-m-1}Y_{l-2}{}^m(\hat{\Omega})]\right.$$

$$- \frac{3}{8\pi}g_{l+1}B_{l+1}{}^{-m-1}[B_{l+2}{}^m Y_{l+2}{}^m(\hat{\Omega})$$

$$- B_{l+1}{}^{-m-1}Y_l{}^m(\hat{\Omega})] + \frac{3}{4\pi}g_{l-1}A_l{}^m[A_l{}^m Y_l{}^m(\hat{\Omega})$$

$$+ A_{l-1}{}^m Y_{l-2}{}^m(\hat{\Omega})] + \frac{3}{4\pi}g_{l+1}A_{l+1}{}^m[A_{l+2}{}^m Y_{l+2}{}^m(\hat{\Omega})$$

$$+ A_{l+1}{}^m Y_l{}^m(\hat{\Omega})] - \frac{3}{8\pi}g_{l-1}B_l{}^{-m}[-B_l{}^{-m}Y_l{}^m(\hat{\Omega})$$

$$+ B_{l-1}{}^{m-1}Y_{l-2}{}^m(\hat{\Omega})] + \frac{3}{8\pi}g_{l+1}B_{l+1}{}^{m-1}$$

$$\left.\times[-B_{l+2}{}^{-m}Y_{l+2}{}^m(\hat{\Omega}) + B_{l+1}{}^{m-1}Y_l{}^m(\hat{\Omega})]\right\} = 0.$$

$$(A15)$$

Next we multiply Eq. (A15) by $Y_{\alpha,\beta}{}^*(\hat{\Omega})$ and integrate over $\hat{\Omega}$. Using the orthogonality relations for the spherical harmonics, we arrive at

$$\mu_t^{(\alpha)}\Gamma_{\alpha,\beta} + g_\alpha k_c\Gamma_{\alpha,\beta} - k_c\left[\frac{1}{2}(g_{\alpha-1}B_\alpha{}^\beta B_\alpha{}^\beta\Gamma_{\alpha,\beta}\right.$$

$$- g_{\alpha+1}B_{\alpha+2}{}^\beta B_{\alpha+1}{}^{-\beta-1}\Gamma_{\alpha+2,\beta})$$

$$- \frac{1}{2}(g_{\alpha-1}B_{\alpha-1}{}^{-\beta-1}B_\alpha{}^\beta\Gamma_{\alpha-2,\beta}$$

$$- g_{\alpha+1}B_{\alpha+1}{}^{-\beta-1}B_{\alpha+1}{}^{-\beta-1}\Gamma_{\alpha,\beta}) + (g_{\alpha-1}A_\alpha{}^\beta A_\alpha{}^\beta\Gamma_{\alpha,\beta}$$

$$+ g_{\alpha+1}A_{\alpha+2}{}^\beta A_{\alpha+1}{}^\beta\Gamma_{\alpha+2,\beta}) + (g_{\alpha-1}A_{\alpha-1}{}^\beta A_\alpha{}^\beta\Gamma_{\alpha-2,\beta}$$

$$+ g_{\alpha+1}A_{\alpha+1}{}^\beta A_{\alpha+1}{}^\beta\Gamma_{\alpha,\beta}) - \frac{1}{2}(-g_{\alpha-1}BB_\alpha{}^{-\beta}B_\alpha{}^{-\beta}$$

$$\times \Gamma_{\alpha,\beta} + g_{\alpha+1}B_{\alpha+2}{}^{-\beta}B_{\alpha+1}{}^{\beta-1}\Gamma_{\alpha+2,\beta})$$

$$+ \frac{1}{2}(-g_{\alpha-1}B_{\alpha-1}{}^{\beta-1}B_\alpha{}^{-\beta}\Gamma_{\alpha-2,\beta}$$

$$\left.+ g_{\alpha+1}B_{\alpha+1}{}^{\beta-1}B_{\alpha+1}{}^{\beta-1}\Gamma_{\alpha,\beta})\right] + \frac{1}{2}B_{\alpha+1}{}^{\beta-1}$$

$$\times\left(\frac{\partial}{\partial x} - i\frac{\partial}{\partial y}\right)\Gamma_{\alpha+1,\beta-1} - \frac{1}{2}B_\alpha{}^{-\beta}\left(\frac{\partial}{\partial x} - i\frac{\partial}{\partial y}\right)$$

$$\times \Gamma_{\alpha-1,\beta-1} - \frac{1}{2}B_{\alpha+1}{}^{-\beta-1}\left(\frac{\partial}{\partial x} + i\frac{\partial}{\partial y}\right)$$

$$\times \Gamma_{\alpha+1,\beta+1} + \frac{1}{2}B_\alpha{}^\beta\left(\frac{\partial}{\partial x} + i\frac{\partial}{\partial y}\right)\Gamma_{\alpha-1,\beta+1}$$

$$+ A_{\alpha+1}{}^\beta\frac{\partial}{\partial z}\Gamma_{\alpha+1,\beta} + A_\alpha{}^\beta\frac{\partial}{\partial z}\Gamma_{\alpha-1,\beta} = q_{\alpha,\beta}. \quad (A16)$$

This is a coupled set of linear differential equations for $\Gamma_{\alpha,\beta}$.

To obtain the correlation diffusion equation, we neglect all the $\Gamma_{\alpha,\beta}$ and g_α values for $\alpha > 1$. The $\alpha = 0$ equation is

$$\mu_a\Gamma_{0,0} + k_c(1 - g_1)\Gamma_{0,0} + \frac{1}{2}\sqrt{\frac{2}{3}}\left(\frac{\partial}{\partial x} - i\frac{\partial}{\partial y}\right)\Gamma_{1,-1}$$

$$- \frac{1}{2}\sqrt{\frac{2}{3}}\left(\frac{\partial}{\partial x} + i\frac{\partial}{\partial y}\right)\Gamma_{1,1} + \sqrt{\frac{1}{3}}\frac{\partial}{\partial z}\Gamma_{1,0} = q_{0,0},$$

$$(A17)$$

and the $\alpha = 1$ equations are

$$\mu_t^{(1)}\Gamma_{1,-1} + (g_1 - 1/3)k_c\Gamma_{1,-1} + \frac{1}{2}\sqrt{\frac{2}{3}}\left(\frac{\partial}{\partial x} + i\frac{\partial}{\partial y}\right)\Gamma_{0,0}$$

$$= q_{1,-1}, \quad (A18)$$

$$\mu_t^{(1)}\Gamma_{1,0} + (g_1 - 1/3)k_c\Gamma_{1,0} + \sqrt{\frac{1}{3}}\frac{\partial}{\partial z}\Gamma_{0,0} = q_{1,0}, \quad (A19)$$

$$\mu_t^{(1)}\Gamma_{1,1} + (g_1 - 1/3)k_c\Gamma_{1,1} - \frac{1}{2}\sqrt{\frac{2}{3}}\left(\frac{\partial}{\partial x} - i\frac{\partial}{\partial y}\right)\Gamma_{0,0}$$

$$= q_{1,1}. \quad (A20)$$

Using the definition for the correlation fluence $G_1(\mathbf{r}, \tau)$ [Eq. (A2)] and the correlation flux $\mathbf{J}_g(\mathbf{r}, \tau)$ [Eq. (A3)], we can rewrite the $\alpha = 0$ and $\alpha = 1$ equations as

$$\mu_a G_1(\mathbf{r}, \tau) + \tfrac{1}{3}\, \mu_s' k_o^2 \langle \Delta r^2(\tau) \rangle G_1(\mathbf{r}, \tau) + \nabla \cdot \mathbf{J}_g(\mathbf{r}, \tau)$$
$$= S_0(\mathbf{r}), \quad \text{(A21)}$$

$$\mu_t^{(1)} \mathbf{J}_g(\mathbf{r}, \tau) + \tfrac{1}{3}\, \mu_s(g_1 - \tfrac{1}{3}) k_o^2 \langle \Delta r^2(\tau) \rangle \mathbf{J}_g(\mathbf{r}, \tau)$$
$$+ \tfrac{1}{3}\nabla G_1(\mathbf{r}, \tau) = \mathbf{S}_1(\mathbf{r}). \quad \text{(A22)}$$

Recall that we have assumed that correlation $G_1{}^T(\mathbf{r}, \hat{\Omega}, \tau)$ is nearly isotropic and that the scattering particles have moved a distance that is much smaller than a wavelength of light. The first assumption is satisfied when $\mu_a \ll \mu_s$ and when the scattering is not too anisotropic. The second assumption is satisfied when $k_o^2 \langle \Delta r^2(\tau) \rangle \ll 1$. To keep our equations consistent with these approximations it is necessary to drop terms from Eq. (A22); in particular,

$$\mu_s' \mathbf{J}_g(\mathbf{r}, \tau) + \tfrac{1}{3}\nabla G_1(\mathbf{r}, \tau) = \mathbf{S}_1(\mathbf{r}). \quad \text{(A23)}$$

Decoupling Eqs. (A21) and (A23) for $G_1(\mathbf{r}, \tau)$, we arrive at the correlation diffusion equation

$$\left[-\nabla \cdot \left(\frac{1}{v} D_\gamma \nabla \right) + \mu_a + \frac{1}{3}\, \mu_s' k_o^2 \langle \Delta r^2(\tau) \rangle \right] G_1(\mathbf{r}, \tau)$$
$$= S_0(\mathbf{r}) - \nabla \cdot \left[\frac{3}{v} D_\gamma \mathbf{S}_1(\mathbf{r}) \right], \quad \text{(A24)}$$

where $D_\gamma = v/(3\mu_s')$ is the photon-diffusion coefficient.

ACKNOWLEDGMENTS

*Present address, Electro-Optic Technology Center, Tufts University, Medford, Massachusetts 02155.

REFERENCES

1. A. Yodh and B. Chance, "Spectroscopy and imaging with diffusing light," Phys. Today **48**, 34–40 (1995).
2. B. Chance, ed., *Photon Migration in Tissues* (Plenum, New York, 1989).
3. B. J. Tromberg, L. O. Svaasand, T. Tsay, and R. C. Haskell, "Properties of photon density waves in multiple-scattering media," Appl. Opt. **32**, 607–616 (1993).
4. M. S. Patterson, B. Chance, and B. C. Wilson, "Time resolved reflectance and transmittance for the non-invasive measurement of tissue optical properties," Appl. Opt. **28**, 2331–2336 (1989).
5. G. A. Millikan, "Experiments on muscle haemoglobin *in vivo*: the instantaneous measurement of muscle metabolism," Proc. R. Soc. London, Sect. B **129**, 218–241 (1937).
6. G. A. Millikan, "The oximeter, an instrument for measuring continuously the oxygen saturation of arterial blood in man," Rev. Sci. Instrum. **13**, 434–444 (1942).
7. F. F. Jobsis, "Noninvasive, infrared monitoring of cerebral and myocardial oxygen sufficiency and circulatory parameters," Science **198**, 1264–1267 (1977).
8. J. M. Schmitt, "Simple photon diffusion analysis of the effects of multiple scattering on pulse oximetry," IEEE Trans. Biomed. Eng. **38**, 1194–1203 (1991).
9. M. R. Neuman, "Pulse oximetry: physical principles technical realization and present limitations," Adv. Exp. Med. Biol. **220**, 135–144 (1987).
10. J. W. Severinghaus, "History and recent developments in pulse oximetry," Scand. J. Clin. Lab. Invest. **53**, 105–111 (1993).
11. W. F. Cheong, S. A. Prahl, and A. J. Welch, "A review of the optical properties of biological tissues," IEEE J. Quantum Electron. **26**, 2166–2185 (1990).
12. B. C. Wilson, E. M. Sevick, M. S. Patterson, and B. Chance, "Time-dependent optical spectroscopy and imaging for biomedical applications," Proc. IEEE **80**, 918–930 (1992).
13. See related studies by S. R. Arridge *et al.*, J. P. Kaltenbach *et al.*, and R. L. Barbour *et al.*, in *Medical Optical Tomography: Functional Imaging and Monitoring*, G. Müller, B. Chance, R. Alfano, S. Arridge, J. Beuthan, E. Gratton, M. Kaschke, B. Masters, S. Svanberg, and P. van der Zee, eds., Institute Series of SPIE Optical Engineering (Society of Photo-Optical Instrumentation Engineers, Bellingham, Wash., 1993), pp. 31–143.
14. S. R. Arridge, P. van der Zee, M. Cope, and D. T. Delpy, "Reconstruction methods for infra-red absorption imaging," in *Time-Resolved Spectroscopy and Imaging of Tissues*, B. Chance, ed., Proc. SPIE **1431**, 204–215 (1991).
15. S. P. Gopinath, C. S. Robertson, R. G. Grossman, and B. Chance, "Near-infrared spectroscopic localization of intracranial hematomas," J. Neurosurg. **79**, 43–47 (1993).
16. A. P. Shepherd and P. A. Oberg, eds., *Laser-Doppler Blood Flowmetry* (Kluwer Academic, Boston, Mass., 1990).
17. L. E. Drain, *The Laser Doppler Technique* (Wiley, New York, 1980).
18. G. V. Belcaro, U. Hoffmann, A. Bollinger, and A. N. Nicolaides, eds., *Laser Doppler* (Med-Orion, London, 1994).
19. A. D. Edwards, C. Richardson, P. van der Zee, M. Cope, and D. T. Delpy, "Measurement of hemoglobin flow and blood flow by near-infrared spectroscopy," J. Appl. Physiol. **75**, 1884–1889 (1993).
20. N. A. Clark, J. H. Lunacek, and G. B. Benedek, "A study of Brownian motion using light scattering," Am. J. Phys. **38**, 575–585 (1970).
21. P. J. Berne and R. Pecora, *Dynamic Light Scattering* (Wiley, New York, 1976).
22. B. J. Berne and R. Pecora, in *Dynamic Light Scattering with Applications to Chemistry, Biology, and Physics* (Krieger, Malabar, Fla., 1990).
23. W. Brown, ed., *Dynamic Light Scattering: The Method and Some Applications* (Clarendon, New York, 1993).
24. G. G. Fuller, J. M. Rallison, R. L. Schmidt, and L. G. Leal, "The measurement of velocity gradients in laminar flow by homodyne light-scattering spectroscopy," J. Fluid Mech. **100**, 555–575 (1980).
25. P. Tong, W. I. Goldburg, C. K. Chan, and A. Sirivat, "Turbulent transition by photon-correlation spectroscopy," Phys. Rev. A **37**, 2125–2133 (1988).
26. M. Bertolotti, B. Crosignani, P. Di, Porto, and D. Sette, "Light scattering by particles suspended in a turbulent fluid, " J. Phys. A **2**, 126–128 (1969).
27. P. J. Bourke, J. Butterworth, L. E. Drain, P. A. Egelstaff, E.

Jakeman, and E. R. Pike, "A study of the spatial structure of turbulent flow by intensity-fluctuation spectroscopy," J. Phys. A **3**, 216–228 (1970).

28. T. Tanaka, C. Riva, and I. Ben-Sira, "Blood velocity measurements in human retinal vessels," Science **186**, 830–831 (1974).

29. M. Stern, "*In vivo* evaluation of microcirculation by coherent light scattering," Nature (London) **254**, 56–58 (1975).

30. R. Bonner and R. Nossal, "Model for laser Doppler measurements of blood flow in tissue," Appl. Opt. **20**, 2097–2107 (1981).

31. H. Z. Cummings and E. R. Pike, eds., *Photon Correlation and Light-Beating Spectroscopy*, Vol. 3 of NATO Advanced Study Institute Series B: Physics (Plenum, New York, 1974).

32. D. J. Pine, D. A. Weitz, P. M. Chaikin, and E. Herbolzheimer, "Diffusing-wave spectroscopy," Phys. Rev. Lett. **60**, 1134–1137 (1988).

33. F. C. MacKintosh and S. John, "Diffusing-wave spectroscopy and multiple scattering of light in correlated random media," Phys. Rev. B **40**, 2382–2406 (1989).

34. G. Maret and P. E. Wolf, "Multiple light scattering from disordered media. The effect of Brownian motion of scatterers," Z. Phys. B **65**, 409–413 (1987).

35. A. Y. Val'kov and V. P. Romanov, "Characteristics of propagation and scattering of light in nematic liquid crystals," Sov. Phys. JETP **63**, 737–743 (1986) [Zh. Eksp. Teor. Fiz. **90**, 1264–1274 (1986)].

36. P. N. Pusey and J. M. Vaughan, "Light scattering and intensity fluctuation spectroscopy," in *Specialist Periodical Report*, Vol. 2 of *Dielectric and Related Molecular Processes*. M. Davies, ed. (The Chemical Society, London, 1975).

37. S. O. Rice, "Mathematical analysis of random noise," in *Noise and Stochastic Processes*, N. Wax, ed. (Dover, New York, 1954), p. 133.

38. D. A. Boas, L. E. Campbell, and A. G. Yodh, "Scattering and imaging with diffusing temporal field correlations," Phys. Rev. Lett. **75**, 1855–1858 (1995).

39. D. A. Boas, "Diffuse photon probes of structural and dynamical properties of turbid media: theory and biomedical applications," Ph.D. dissertation (Department of Physics and Astronomy, University of Pennsylvania, Philadelphia, Pa., 1996).

40. D. A. Boas, I. V. Meglinsky, L. Zemany, L. E. Campbell, B. Chance, and A. G. Yodh, "Diffusion of temporal field correlation with selected applications," in *Coherence-Domain Methods in Biomedical Optics*, V. V. Tuchin, ed., Proc. SPIE **2732**, 34–46 (1996).

41. D. A. Weitz, D. J. Pine, P. N. Pusey, and R. J. A. Tough, "Nondiffusive Brownian motion studied by diffusing-wave spectroscopy," Phys. Rev. Lett. **63**, 1747–1750 (1989).

42. X. Qiu, X. L. Wu, J. Z. Xue, D. J. Pine, D. A. Weitz, and P. M. Chaikin, "Hydrodynamic interactions in concentrated suspensions," Phys. Rev. Lett. **65**, 516–518 (1990).

43. P. D. Kaplan, A. G. Yodh, and D. J. Pine, "Diffusion and structure in dense binary suspensions." Phys. Rev. Lett. **68**, 393–396 (1992).

44. J. X. Zhu, D. J. Durian, J. Muller, D. A. Weitz, and D. J. Pine, "Scaling of transient hydrodynamic interactions in concentrated suspensions," Phys. Rev. Lett. **68**, 2559–2562 (1992).

45. M. H. Kao, A. G. Yodh, and D. J. Pine, "Observation of Brownian motion on the time scale of hydrodynamic interactions," Phys. Rev. Lett. **70**, 242–245 (1993).

46. S. J. Nilsen and A. P. Gast, "The influence of structure on diffusion in screened Coulombic suspensions," J. Chem. Phys. **101**, 4975–4985 (1994).

47. A. J. C. Ladd, H. Gang, J. X. Zhu, and D. A. Weitz, "Time-dependent collective diffusion of colloidal particles," Phys. Rev. Lett. **74**, 318–321 (1995).

48. D. J. Durian, D. A. Weitz, and D. J. Pine, "Multiple light scattering probes of foam structure and dynamics," Science **252**, 686–688 (1991).

49. A. D. Gopal and D. J. Durian, "Nonlinear bubble dynamics in a slowly driven foam," Phys. Rev. Lett. **75**, 2610–2613 (1995).

50. H. Gang, A. H. Krall, and D. A. Weitz, "Shape fluctuations of interacting fluid droplets," Phys. Rev. Lett. **73**, 3435–3438 (1994).

51. P. D. Kaplan, A. G. Yodh, and D. F. Townsend, "Noninvasive study of gel formation in polymer-stabilized dense colloids using multiply scattered light," J. Colloid Interface Sci. **155**, 319–324 (1993).

52. J. D. Briers, "Laser Doppler and time-varying speckle: a reconciliation," J. Opt. Soc. Am. A **13**, 345–350 (1996).

53. H. Z. Cummings and H. L. Swinney, "Light beating spectroscopy," Prog. Opt. **8**, 133–200 (1970).

54. P. N. Pusey, J. M. Vaughan, and D. V. Willets, "Effect of spatial incoherence of the laser in photon-counting spectroscopy," J. Opt. Soc. Am. **73**, 1012–1017 (1983).

55. T. Bellini, M. A. Glaser, N. A. Clark, and V. Degiorgio, "Effects of finite laser coherence in quasielastic multiple scattering," Phys. Rev. A **44**, 5215–5223 (1991).

56. X. L. Wu, D. J. Pine, P. M. Chaikin, J. S. Huang, and D. A. Weitz, "Diffusing-wave spectroscopy in a shear flow," J. Opt. Soc. Am. B **7**, 15–20 (1990).

57. D. J. Pine, D. A. Weitz, J. X. Zhu, and E. Herbolzheimer, "Diffusing-wave spectroscopy: dynamic light scattering in the multiple scattering limit," J. Phys. (Paris) **51**, 2101–2127 (1990).

58. K. Katayama, G. Nishimura, M. Kinjo, and M. Tamura, "Absorbance measurements in turbid media by the photon correlation method," Appl. Opt. **34**, 7419–7427 (1995).

59. G. Nishimura, K. Katayama, M. Kinjo, and M. Tamura, "Diffusing-wave absorption spectroscopy in the homogeneous turbid media," Opt. Commun. **128**, 99–107 (1996).

60. M. J. Stephen, "Temporal fluctuations in wave propagation in random media," Phys. Rev. B **37**, 1–5 (1988).

61. B. J. Ackerson, R. L. Dougherty, N. M. Reguigui, and U. Nobbman, "Correlation transfer: application of radiative transfer solution methods to photon correlation problems," J. Thermophys. Heat Transfer **6**, 577–588 (1992).

62. R. L. Dougherty, B. J. Ackerson, N. M. Reguigui, F. Dorri-Nowkoorani, and U. Nobbmann, "Correlation transfer: development and application," J. Quant. Spectrosc. Radiat. Transfer. **52**, 713–727 (1994).

63. S. Chandrasekhar, *Radiative Transfer* (Dover, New York, 1960).

64. A. Ishimaru, *Wave Propagation and Scattering in Random Media* (Academic, New York, 1978).

65. H. S. Carslaw and J. Jaeger, *Conduction of Heat in Solids* (Oxford U. Press, New York, 1986).

66. H. C. van de Hulst, *Light Scattering by Small Particles* (Dover, New York, 1981).

67. J. Z. Xue, D. J. Pine, S. T. Milner, X. L. Wu, and P. M. Chaikin, "Nonergodicity and light scattering from polymer gels," Phys. Rev. A **46**, 6550–6563 (1992).

68. K. Schatzel, "Accuracy of photon correlation measurements on nonergodic samples," Appl. Opt. **32**, 3880–3885 (1993).

69. J. G. H. Joosten, E. T. F. Gelade, and P. N. Pusey, "Dynamic light scattering by nonergodic media: Brownian particles trapped in polyacrylamide gels," Phys. Rev. A **42**, 2161–2175 (1990).

70. P. N. Pusey and W. Van Megen, "Dynamic light scattering by non-ergodic media," Physica A **157**, 705–742 (1989).

71. E. R. Van Keuren, H. Wiese, and D. Horn, "Diffusing-wave spectroscopy in concentrated latex dispersions: an investigation using single-mode fibers," Colloids Surf. A **77**, 29–37 (1993).

72. J. Ricka, "Dynamic light scattering with single-mode and multimode fibers," Appl. Opt. **32**, 2860–2875 (1993).

73. R. G. Brown, "Dynamic light scattering using monomode optical fibers," Appl. Opt. **26**, 4846–4851 (1987).

74. A. A. Middleton and D. S. Fisher, "Discrete scatterers and autocorrelations of multiply scattered light," Phys. Rev. B **43**, 5934–5938 (1991).

75. D. J. Durian, "Accuracy of diffusing-wave spectroscopy theories," Phys. Rev. E **51**, 3350–3358 (1995).

76. M. H. Koelink, F. F. M. de Mul, J. Greve, R. Graaff, A. C. M. Dassel, and J. G. Aarnoudse, "Laser Doppler blood flow-metry using two wavelengths: Monte Carlo simulations and measurements," Appl. Opt. **33**, 3549–3558 (1994).

77. R. Graaff, M. H. Koelink, F. F. M. de Mul, W. G. Zijlstra, A. C. M. Dassel, and J. G. Aarnoudse, "Condensed Monte Carlo simulations for the description of light transport," Appl. Opt. **32**, 426–434 (1993).

78. S. L. Jacques and L. Wang, "Monte Carlo modeling of light transport in tissues," in *Optical-Thermal Response of Laser-Irradiated Tissue*, A. J. Welch and M. J. C. van Gemert, eds. (Plenum, New York, 1995), pp. 73–100.

79. L. Wang, S. L. Jacques, and L. Zheng, "MCML-Monte Carlo modeling of light transport in multi-layered tissues," Comput. Methods Prog. Biomed. **47**, 131–146 (1995).

80. L. G. Henyey and J. L. Greenstein, "Diffuse radiation in the galaxy," Astrophys. J. **93**, 70–83 (1941).

81. D. A. Boas, M. A. O'Leary, B. Chance, and A. G. Yodh, "Scattering of diffuse photon density waves by spherical inhomogeneties within turbid media: analytic solution and applications," Proc. Natl. Acad. Sci. USA **91**, 4887–4891 (1994).

82. P. N. den Outer, T. M. Nieuwenhuizen, and A. Lagendijk, "Location of objects in multiple-scattering media," J. Opt. Soc. Am. A **10**, 1209–1218 (1993).

83. R. C. Haskell, L. O. Svaasand, T. Tsay, T. Feng, M. S. McAdams, and B. J. Tromberg, "Boundary conditions for the diffusion equation in radiative transfer," J. Opt. Soc. Am. A **11**, 2727–2741 (1994).

84. A. C. Kak and M. Slaney, in *Principles of Computerized Tomographic Imaging* (Institute of Electrical and Electronics Engineers, New York, 1988).

85. R. Nossal, S. H. Chen, and C. C. Lai, "Use of laser scattering for quantitative determinations of bacterial motility," Opt. Commun. **4**, 35–39 (1971).

86. D. Bicout and R. Maynard, "Diffusing wave spectroscopy in inhomogeneous flows," Physica A **199**, 387–411 (1993).

87. D. Bicout and G. Maret, "Multiple light scattering in Taylor–Couette flow," Physica A **210**, 87–112 (1994).

88. D. J. Bicout and R. Maynard, "Multiple light scattering in turbulent flow," Physica B **204**, 20–26 (1995).

89. D. Bicout, "Non-Newtonian behavior of colloidal suspensions from multiple light scattering," Phys. Lett. A **180**, 375–378 (1993).

90. The Intralipid used here can be obtained from Kabi Pharmacia, Clayton, North Carolina.

91. R. Nossal, R. F. Bonner, and G. H. Weiss, "Influence of path length on remote optical sensing of properties of biological tissue," Appl. Opt. **28**, 2238–2244 (1989).

92. H. A. Green, E. E. Burd, N. S. Nishioka, and C. C. Compton, "Skin-graft take and healing following 193-nm excimer, continuous-wave carbon dioxide (CO_2), pulsed CO_2, or pulsed holmium-YAG laser-ablation of the graft bed," Arch. Dermatol. **129**, 979–988 (1993).

93. K. M. Case and P. F. Zweifel, *Linear Transport Theory* (Addison-Wesley, Reading, Mass., 1967).

94. B. Davison and J. B. Sykes, *Neutron Transport Theory* (Oxford U. Press, London, 1957).

95. S. Glasstone and M. C. Edlund, *The Elements of Nuclear Reactor Theory* (Van Nostrand, Princeton, N.J., 1952).

96. J. M. Kaltenbach and M. Kaschke, "Frequency and time domain modelling of light transport in random media," in *Medical Optical Imaging: Functional Imaging and Monitoring*, Institute Series of SPIE Optical Engineering (Society of Photo-Optical Instrumentation Engineers, Bellingham, Wash., 1993), pp. 65–86.

97. J. D. Jackson, *Classical Electrodynamics* (Wiley, New York, 1975), Chap. 3.6.

98. G. B. Arfken, in *Mathematical Methods for Physicists* (Academic, Orlando, Fla., 1985), Chap. 12.9.